



Instrument Science Report WFC3 2025-09

Testing and Validation of the Updated Pixel-Based Non-Linearity Calibration File for WFC3/IR

K. Huynh, V. Bajaj, M. Marinelli, J. Mack, S. Shenoy, N. Grogan

November 4, 2025

Last Updated: February 4, 2026

ABSTRACT

The WFC3/IR channel has an innate non-linear response to incident photons, which is corrected for in the `calwf3` pipeline with the `NLINFILE` reference file. The 2009 solution is based on an average polynomial correction for each IR quadrant and is found to be poorly constrained at high fluence levels (e^-) approaching the saturation limit. Using a variety of image types, sources, and sample sequences, we test a new pixel-based linearity correction developed by Shenoy et al. (2025). In nearly all cases, the new correction improves the linearity at fluence levels higher than $\sim 50,000 e^-$, with improvements up to 7% for pixels with fluences approaching the saturation limit ($\sim 80,000 e^-$) in the last `ima` reads. The pixel-based solution also significantly decreases the number of cosmic rays erroneously flagged (due to non-linearity correction errors) during ramp fitting in `calwf3`, leading to improved photometric accuracy in the calibrated `flt` data and higher signal-to-noise ratios, particularly in Quad 1 (upper-left detector quadrant). Because the new solution tends to make sources brighter, we recalibrate the five HST flux standards used to compute the IR zeropoints and find a negligible impact ($\sim 0.1\text{--}0.2\%$) on the published values by Calamida et al. (2024), smaller than the RMS dispersion ($\sim 0.5\%$) in the observed to synthetic flux ratios for all five flux standards. The new `NLINFILE 9au15283i.lin.fits` was delivered to CRDS in October 2025 and will be used to reprocess all WFC3/IR imaging and grism observations in the MAST archive.

An updated reference file `a2412448i.lin.fits` was delivered in February 2026, improving the results at the highest fluence levels by a few tenths of a percent. Please consult the Addendum for details.

Introduction

The Wide Field Camera 3 Infrared (WFC3/IR) channel is a HgCdTe detector with an intrinsically non-linear response to incident photons (Hilbert 2008). Pixel counts that are below the saturation threshold of the IR detector and whose measured flux deviates from linearity are currently modeled by a third-order polynomial, which relates the measured and idealized signal. The WFC3 data calibration pipeline, `calwf3`, corrects for this non-linearity using a calibration reference file called the `NLINFILE`. This `NLINFILE` contains the coefficients of a third-order polynomial applied to each pixel on the detector to correct for the non-linear response. The structure and format of the `NLINFILE` is described in more detail in Shenoy et al. (2025).

The 2009 `NLINFILE` (`u1k1727mi.lin.fits`, hereafter referred to as the current correction) uses a set of quadrant-averaged polynomials derived from Tungsten lamp flats acquired on the ground during TV3 testing (Hilbert 2008). These flats were acquired using the `STEP50` sample sequence, in which the signal is sampled more frequently in the early reads and then at uniform 50-second intervals in the later reads¹. This sampling pattern makes it difficult to constrain the non-linearity for pixels at high fluence levels approaching the full well limit. A new pixel-based non-linearity correction file has been derived using on-orbit `SPARS25` internal flat fields from WFC3 calibration (CAL) programs designed to monitor the IR linearity. WFC3 ISR 2025-08 (Shenoy et al. 2025) describes the methodology used to derive the new coefficients and generate the new pixel-based correction file. The aforementioned report also includes a map of the IR full saturation limit for each pixel by Hilbert (2008), populated in the `NODE` extension of the `NLINFILE`. The values in this extension (i.e. saturation levels) are unchanged from the original analysis based on TV3 data.

In this report, we highlight improvements in the new pixel-based non-linearity correction file compared with the quadrant-based solution. We compare the results from testing on various datasets, including internal flat fields, star clusters, and CALSPEC standard stars (imaging and grisms), which are used for HST flux calibration. Finally, we measure changes in the observed count rates for the five flux standards in all 15 IR filters in order to check the absolute flux calibration (zeropoints) computed by Calamida et al. (2024).

Internal Flat Fields

Internal lamp flats (INTFLATS) are useful for measuring detector non-linearity effects because they provide a stable, uniform source of illumination under repeatable conditions. This allows for a precise characterization of how the detector response deviates from a perfectly linear relationship at various fluence levels. We reprocess INTFLAT data taken as part of our annual non-linearity monitoring program with our new correction file in five different sample sequence modes, which sample a range of signal levels: `SPARS25` and `SPARS50`

¹For more information on the predefined sample sequence modes for the WFC3/IR channel, please see the [HST Phase II Proposal Instruction Handbook](#).

at high fluence levels, and SPARS10, STEP25, and RAPID at low fluence levels. Table 1 in the Appendix lists the sample sequences (SAMP-SEQ), the number of reads (NSAMP), the exposure time, rootnames, and proposal IDs of the INTFLAT exposures used to validate the new linearity correction.

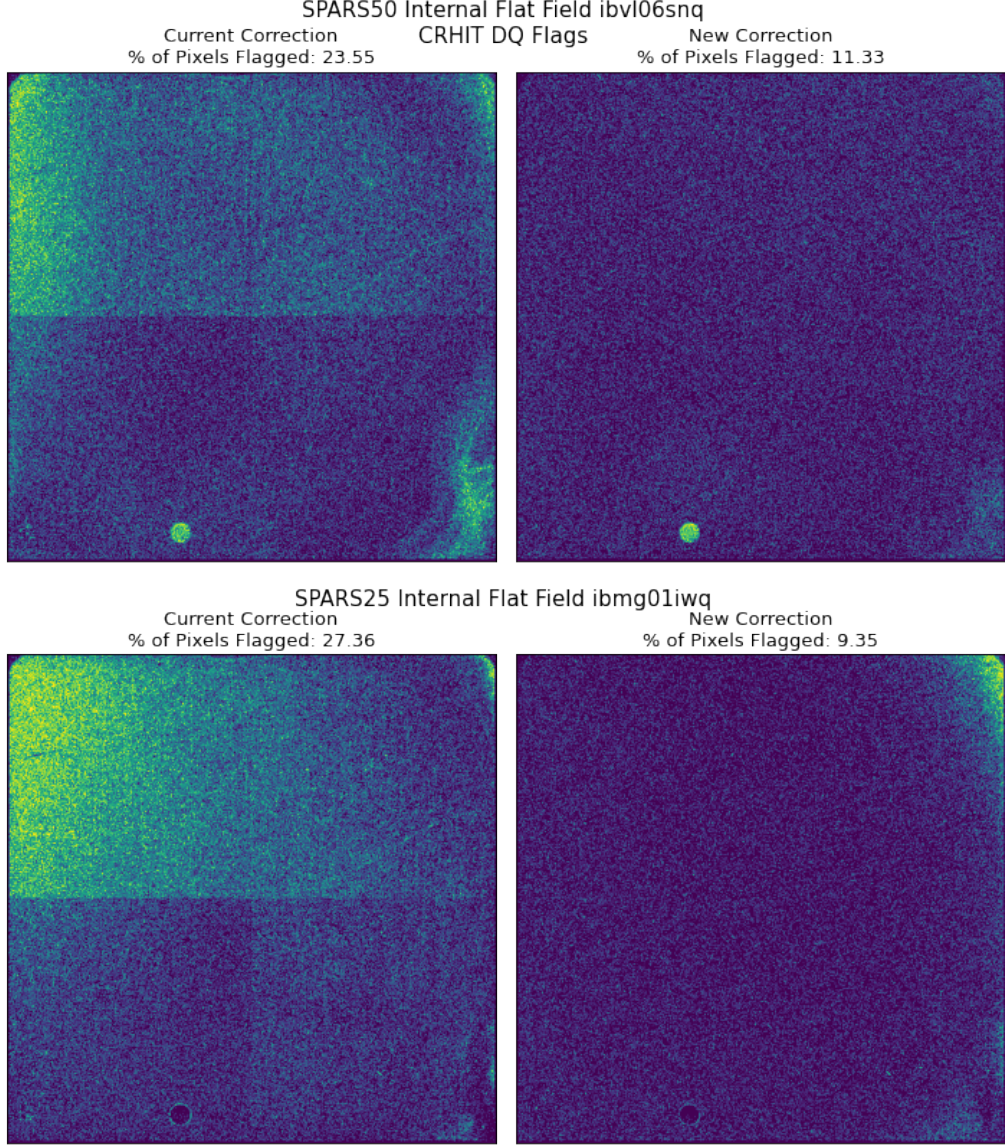


Figure 1: *CRHIT DQ flags in the last *ima* read, e.g. [DQ, 1], for internal flat fields (INTFLATS) acquired with different sample sequences: SPARS50 (*ibvl06snq*) and SPARS25 (*ibmg01iwq*).* For each INTFLAT, the left panel is calibrated with the 2009 quad-based *NLINFILE* and the right panel with the new pixel-based *NLINFILE*. Yellow points show the position of cosmic ray flags ($DQ \geq 8192$) populated by *calwf3* during the up-the-ramp fit. Each panel reports the percentage of detector pixels flagged, with the new solution flagging two times fewer pixels in the SPARS50 INTFLAT, and three times fewer pixels in the SPARS25 INTFLAT. With the new solution, the number of flagged pixels is now similar in all four quadrants.

Cosmic ray flags (hereafter referred to as CRHIT, $DQ = 8192$) are flagged when the pixel's read value is found to experience a "jump" (usually caused by a cosmic ray) and deviates from the linear fit to the calibrated ramp. These pixels are then rejected from the fitting process, with a rejection threshold of 4σ defined by the CRREJTAB reference table (Pagul and Rivera 2024). However, at levels close to saturation, the linear fit deviates from linearity, and thus may cause erroneous flagging of CRHITs in exposures.

Figure 1 shows the CRHIT flags in the last `ima` read for a SPARS50 and SPARS25 INTFLAT calibrated with the new and current linearity corrections. For the SPARS50 INTFLAT, the current linearity correction tends to overflag pixels, with 23% of detector pixels flagged. This is reduced to 11% of detector pixels with the new correction. For the SPARS25 flat, the improvement is even larger, where the current correction flags nearly three times as many pixels (27%) compared to the new correction (9%). This discrepancy likely arises from limitations in the coefficients derived from the heavily saturated STEP50 INTFLATs used to derive the current quadrant-averaged solution, as well as from unmodeled pixel-to-pixel variations within each quadrant. We also note that the majority of the flags are in quadrant 1 (the upper left quadrant of the IR channel). These flags highlight larger deviations in the true pixel-based linearity compared to the quadrant average. We note a spatial pattern in the number of DQ flags for quadrant 1, with the left third being flagged more frequently with the current correction.

We define the instantaneous count rate (e^-/s) between reads as the measured count rate accumulated between two consecutive reads:

$$\frac{Signal_N - Signal_{N-1}}{Time_N - Time_{N-1}} \quad (1)$$

where N is the read number, $Signal$ is the total measured signal of the read (e^-), and $Time$ is the time at which the read is sampled (s). We also define the fluence level (e^-) as the total accumulated signal at a given read:

$$Count\ Rate_N * Time_N \quad (2)$$

Plotting the instantaneous count rate versus the fluence level provides a diagnostic of the IR channel's linearity. For a perfectly linear detector, we expect the instantaneous count rate to be flat as the fluence level rises. This relationship between instantaneous count rate and fluence will be used throughout the remainder of this report to probe the improvements in our correction.

We compute 1.) the ratio between the instantaneous count rate of each read in the `ima` files and the count rate derived from the `f1t` files using the up-the-ramp fit, and 2.) the fluence level for the given ramp read across every pixel for all INTFLATs observed in the five different sample sequences. INTFLAT observations are measured in units of DN, so we take the additional step of multiplying the pixel values by the gain ($2.5\ e^-/DN$) (Gosmeyer and Baggett 2015). We mask saturated pixels according to their DQ flag, then calculate the 3σ clipped mean of the count rate ratio and fluence across the entire flat for each read. Figures 2–6 show the clipped mean count rate ratio versus the clipped mean fluence level across every read for INTFLATs taken with SPARS50, SPARS25, SPARS10, STEP25, and RAPID sample sequences, respectively.

For SPARS50 and SPARS25 INTFLATs, we exclude the last three and four reads, respectively, due to saturation. We find the most significant improvements in the peak-to-peak range (full range from the minimum to the maximum) across all fluence levels when using the new correction in SPARS50, SPARS25, and STEP50 sample sequence modes, with a reduction from 3% to 1%, 7% to 2% (the greatest improvement), and 5% to 2%, for the three sample sequence modes, respectively. This reduction in peak-to-peak range indicates that the new correction improves both the bright and faint ends when compared to the current correction in these sample sequence modes. The peak-to-peak range remains the same between the two non-linearity correction files for both RAPID and SPARS10, varying by 1% and 0.4%, respectively.

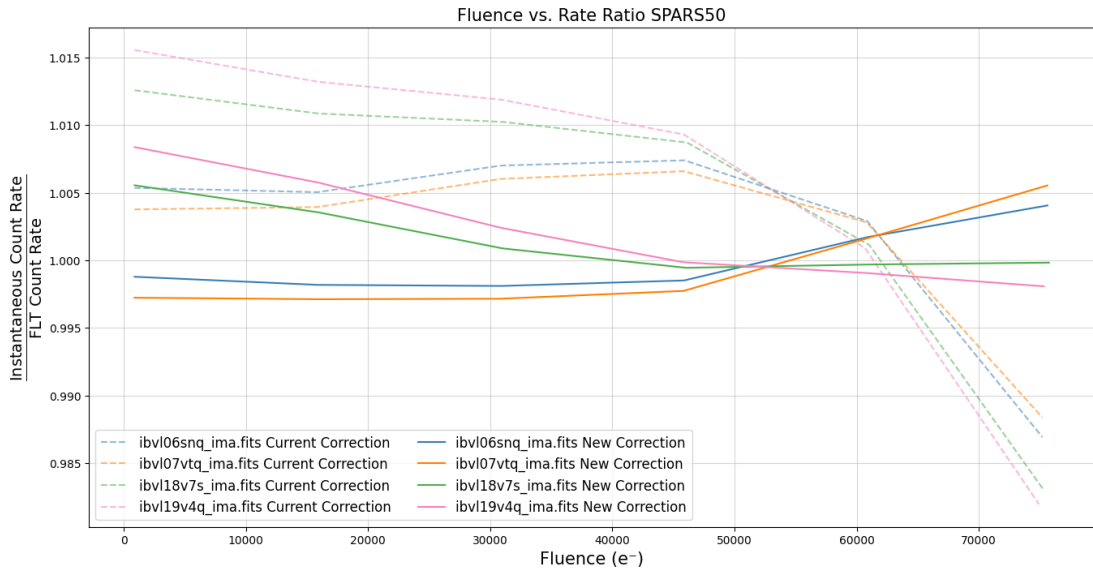


Figure 2: Mean ratio between the *ima* instantaneous count rate and the *flt* count rate vs. the mean fluence level (e^-) for a set of INTFLATs taken in SPARS50 sample sequence. Dashed lines are INTFLATs calibrated with the 2009 *NLINFILE*, while solid lines show ramps calibrated with the new *NLINFILE*. The last four reads are saturated and excluded from the plot. The new correction reduces the peak-to-peak range from $\sim 3\%$ to $\sim 1\%$ across all fluence levels.

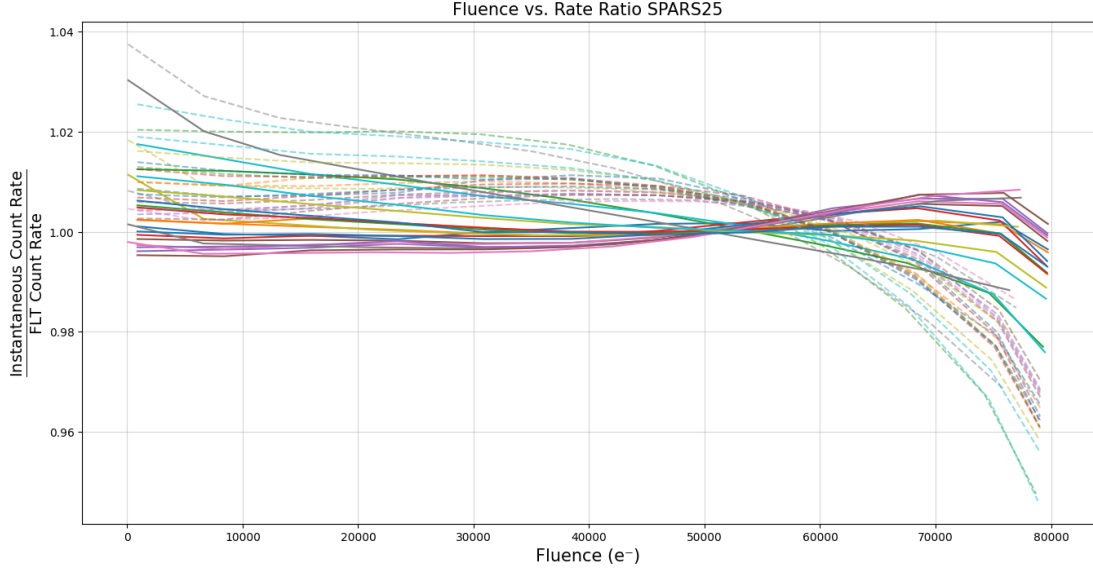


Figure 3: *Same as Figure 2, but for a set of SPARS25 INTFLATS. The last three reads are saturated and excluded from the plot. The new correction reduces the peak-to-peak range from $\sim 6\text{-}7\%$ to $\sim 2\%$, representing the largest improvement observed across all sample sequences tested.*

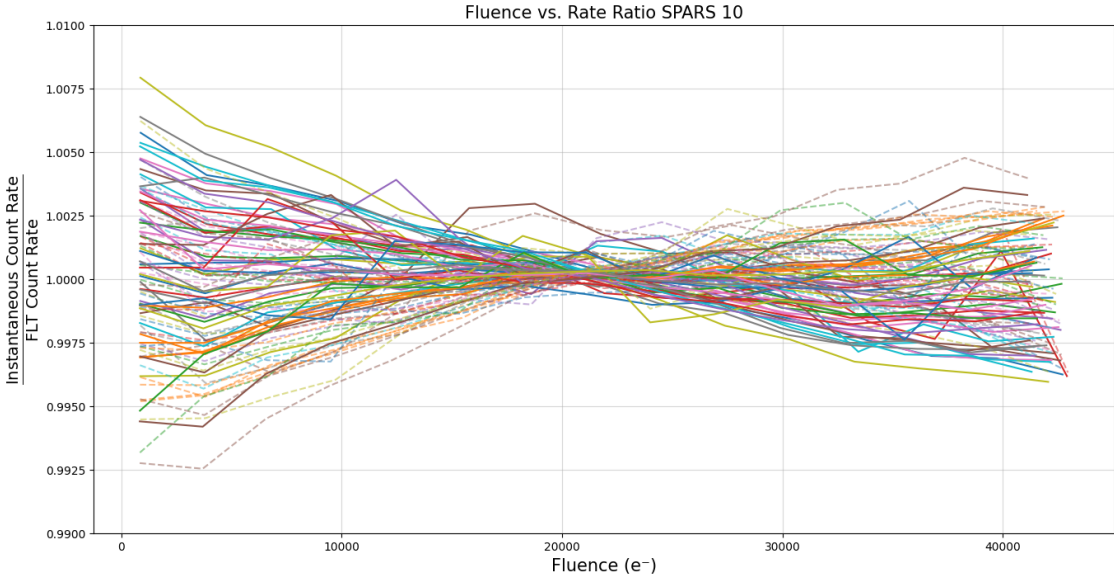


Figure 4: *Same as Figure 2, but for a set of SPARS10 INTFLATS that sample low fluence levels. The peak-to-peak range is $\sim 1\%$ across all fluence levels for both the old and the new corrections.*

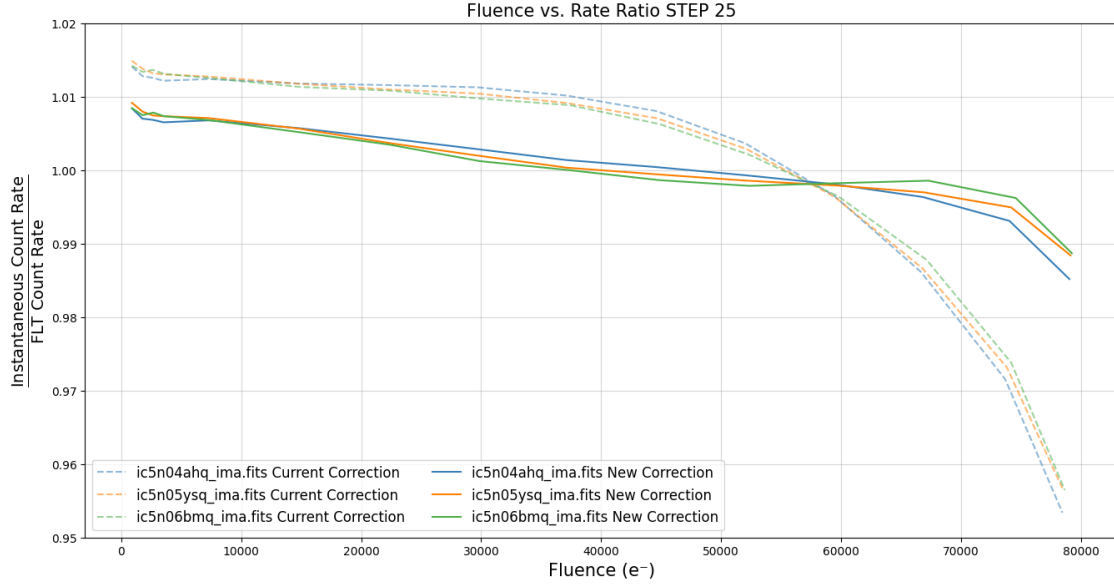


Figure 5: *Same as Figure 2, but for a set of STEP25 INTFLATS. The peak-to-peak range over all fluence levels is reduced from 5% to 2% when using the new linearity correction.*

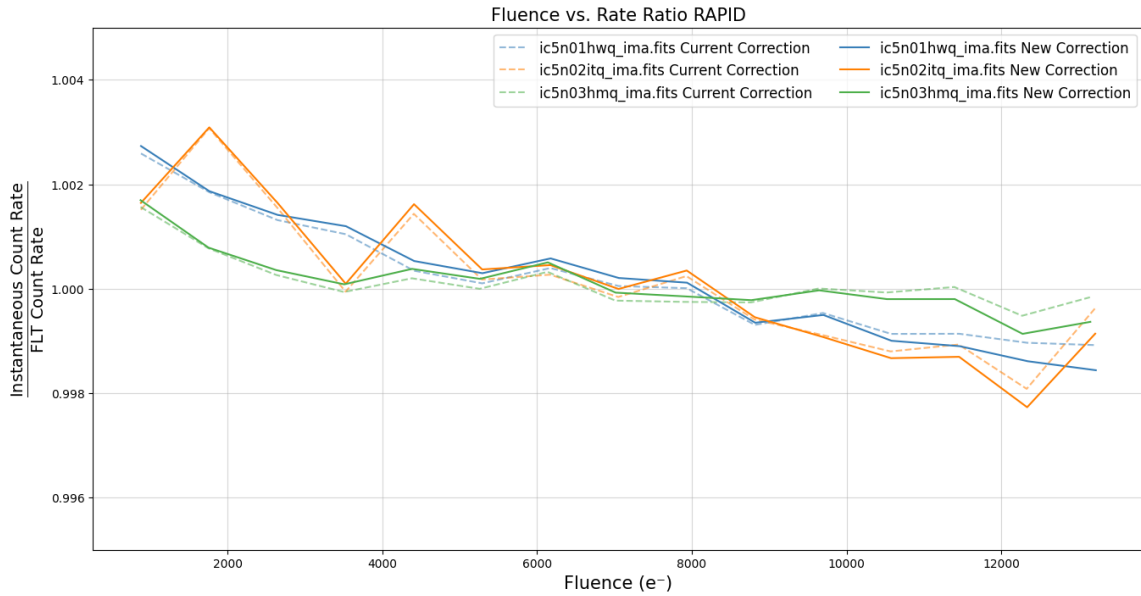


Figure 6: *Same as Figure 2, but for a set of RAPID INTFLATS which sample the lowest fluence levels. The peak-to-peak range remains around 0.4% for both the old and the new correction.*

Star Clusters

NGC1851

We reprocess deep exposures (~ 900 seconds) of a field about three arcmin southwest from the center of globular cluster NGC 1851 (distance ~ 12 kpc), taken in F110W from GO proposal 16177 (PI: Calamida) with our new linearity correction file. Exposures in the visit are taken in non-interruptible sequence mode² and dithered by 8-10 pixels via POS-TARGS, which limits persistence effects (Long et al. 2010).

We identify sources with the `hst1pass` software routine (Anderson 2022) for one F110W exposure `ieaa02e8q` (taken with STEP100 sample sequence with 16 samples). Using the peak pixel value of sources found via `hst1pass`, we identify four sources at different count rates: ~ 75 , 100, 150, and 200 e^-/s . We then plot the instantaneous count rate of the `ima` ramps versus the instantaneous exposure time for the source with the current and new linearity correction file, as shown in Figure 7. In all cases, at later reads where the pixel is approaching saturation, the new linearity correction improves the linearity by $\sim 1\text{-}4\%$.

We also perform 3-pixel radius aperture photometry on sources identified by `hst1pass` in the same exposure. We then plot the percent difference between the measured count rate in the aperture using the two correction files versus the measured count rate with the new correction as shown in Figure 8. At higher count rates (100 e^-/s and higher), the percent difference is 0–0.5%, indicating that the current correction deviates from linearity at the bright end.

²Non-interruptible sequence (`NON-INT`) is a mode in HST’s Astronomer’s Proposal Tool (APT) which flags the observations to be executed back-to-back without any interruptions such as buffer dumps and gaps between Earth’s occultation.

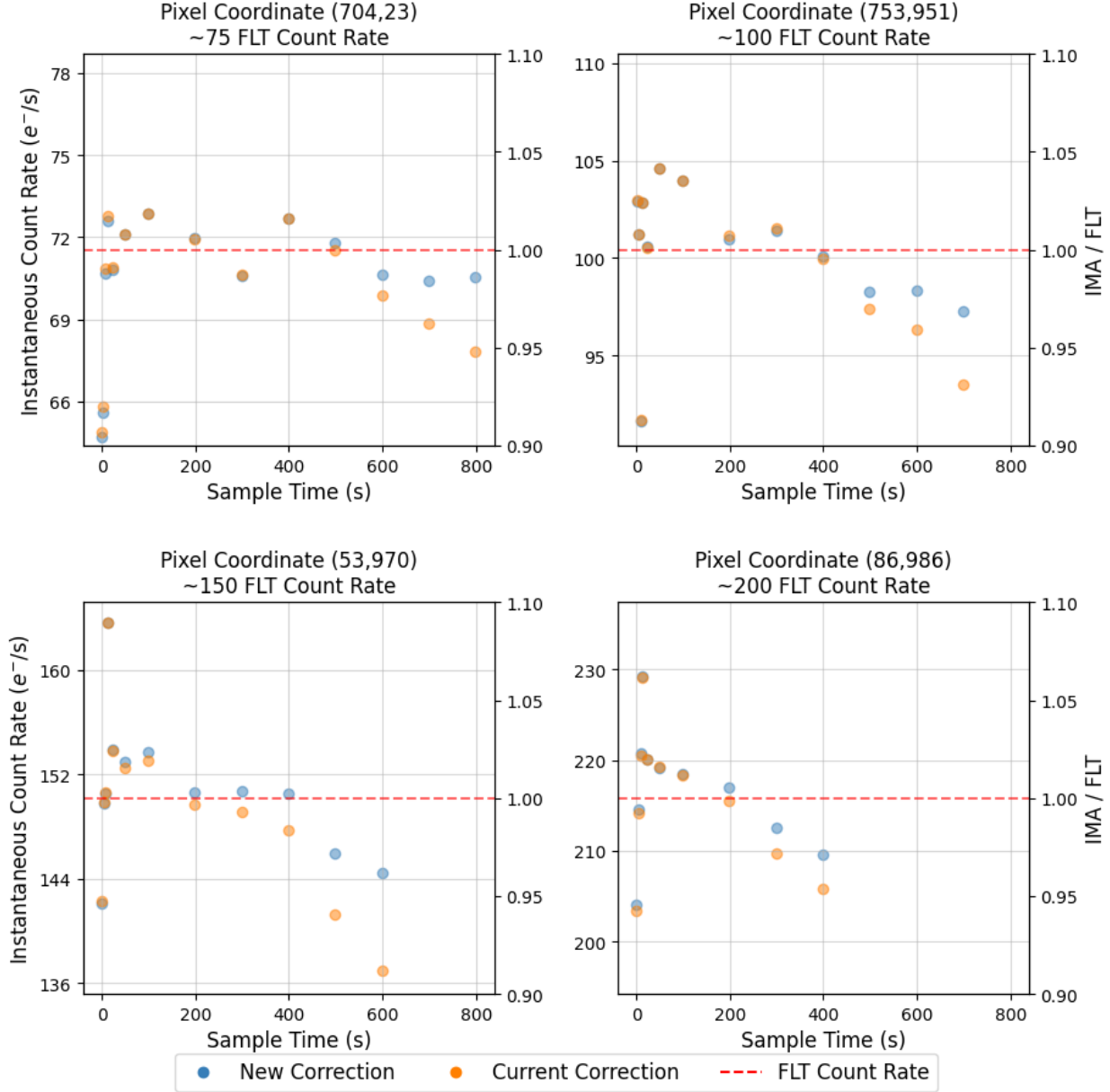


Figure 7: Instantaneous count rate (e^-/s) versus exposure time (s) for the peak pixel of four stars in the globular cluster NGC 1851, acquired in a ~ 900 -second exposure (`ieaa02e8q`) with the `STEP100` sample sequence. Each panel shows changes in the peak pixel value measured across different reads in the `ima` file for stars with different count rates: ~ 75 , 100 , 150 , and 200 e^-/s . Orange points show the shape of the ramp calibrated with the 2009 linearity correction, while blue points show the improvement when using the new linearity correction. For reference, the `flt` count rate derived with the new correction is overplotted as a red dashed line. The 100 , 150 , and 200 count rate ramps reach saturation before the end of the exposure, so their final reads are not shown in the figure. In all four cases, the new linearity correction improves the results by ~ 1 – 4 % at the end of the ramp where the fluence approaches the full well limit.

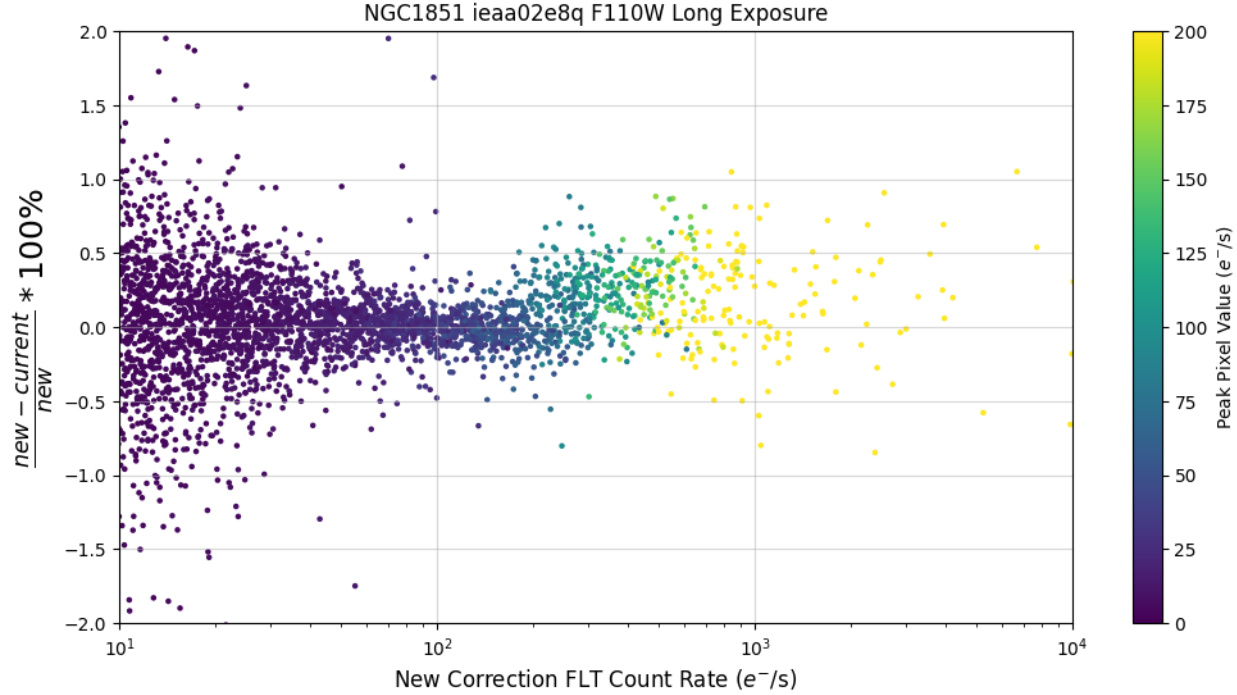


Figure 8: *Percent difference in the `flt` count rate (e^-/s) measured within a 3-pixel radius aperture for stars in NGC 1851 calibrated with the new and current (2009) `NLINFILE` plotted versus the `flt` count rate for the same exposure shown in Figure 7. Points are colored based on their peak pixel value measured via the `hst1pass` software (Anderson 2022). At higher count rates, sources calibrated with the new non-linearity correction files are brighter by up to 0.5% in the 3-pixel aperture compared to the current correction.*

Figure 9 shows the ratio between the instantaneous count rate of `ima` reads and the `flt` count rate value versus the fluence level (e^-) for the peak pixel of sources identified by `hst1pass` with the current and new non-linearity correction (on the same exposure `ieaa02e8q`). We calculate and plot the median-binned statistic with n bins = 15 for reads with a fluence level between 10,000–100,000 e^- , where early reads are excluded due to their scatter. The color of the points indicates whether a DQ flag was populated in the `ima` file during the ramp fitting step, where purple indicates no flag and green shows stars that were flagged as cosmic ray hits in their ramps. In the case of this exposure, only about 1% of pixels are flagged as CRHIT. The current correction deviates from perfect linearity (a count rate ratio of $\sim=1$) at higher fluence levels by $\sim 4\%$, while the new correction improves the deviation from linearity by $\sim 1\text{--}2\%$, reinforcing the improvement at higher fluence levels when using the new pixel-based correction.

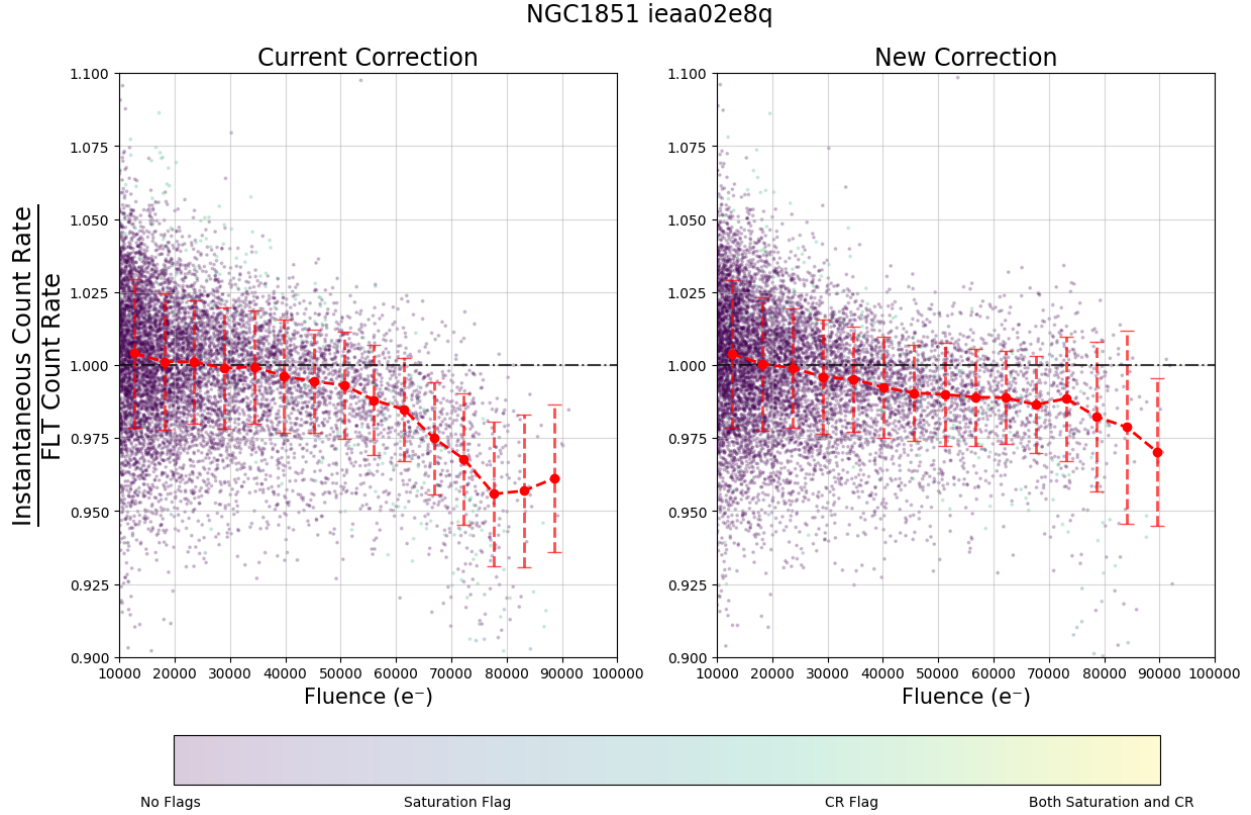


Figure 9: *Ratio of the instantaneous count rate of `ima` reads and the `flt` count rate versus the fluence level (e^-) for the peak pixel of sources identified by `hst1pass` for a ~ 900 -second exposure of NGC 1851 (`ieaa02e8q`) acquired in the F110W filter with the STEP100 sample sequence. The two panels compare the results calibrated with 1.) the current 2009 non-linearity correction file (left) and 2.) the new pixel-based correction (right). Median binned statistics are overplotted for fluence levels between 10,000 and 100,000 e^- , where early reads are excluded due to their large scatter. Points are colored based on their DQ flag populated in the `ima` file during the ramp fitting step, where purple indicates no flag. Only about 1% of sources measured were flagged with CRHIT in this exposure. The new correction improves the linearity by $\sim 1\text{--}2\%$ compared to the current correction at higher fluence levels for sources identified by `hst1pass`.*

47 Tucanae

We repeat the analysis done with NGC 1851 in Figure 9 with 47 Tucanae (a globular cluster at ~ 4.5 kpc) using `if5i02h2q`, a ~ 350 -second F160W exposure acquired with the SPARS25 sample sequence from the WFC3 calibration (CAL) program 17363. While the goal of this program is to monitor the WFC3/IR time-dependent sensitivity with cluster observations (Bajaj et al. 2022), this program duplicates the observing strategy from the prior “WFC3/IR Signal Non-Linearity Monitor,” which was designed to test the linearity correction derived from internal flats using star cluster data (see programs 12352, 12696, 13079, and 13563) and thus is useful for our purpose here.

Figure 10 shows the ratio of the instantaneous count rate of `ima` reads and the `flt` count rate versus the fluence level (e^-) for the peak pixel of sources identified by `hst1pass` for 47 Tucanae exposure `if5i02h2q`. The two panels show the results calibrated with the current and new non-linearity corrections (same analysis as Figure 9). Points are colored based on their DQ flag in the same way as Figure 9. The current correction deviates from linearity at higher fluence levels by up to $\sim 7\%$, while the new correction significantly improves the linearity, deviating only by $\sim 2\%$ at saturated fluence levels.

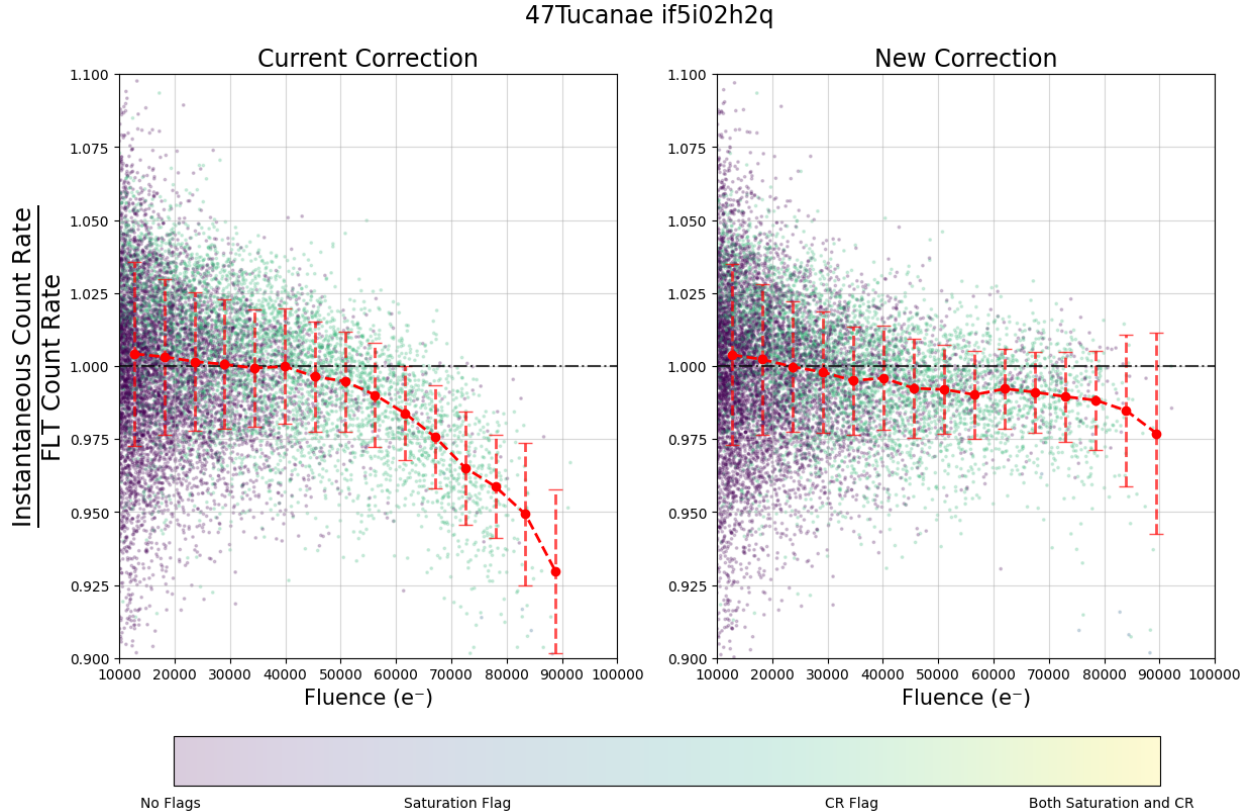


Figure 10: *Same as Figure 9, but for a ~ 350 -second exposure of 47 Tucanae (`if5i02h2q`) acquired in the F160W filter with the SPARS25 sample sequence. The current (2009) correction deviates from linearity at higher fluence levels by up to $\sim 7\%$, while the new correction deviates only by $\sim 2\%$ at the same fluence levels, significantly improving the linearity of the peak pixel of sources. The colorbar indicates whether a flag was populated in the DQ array of the `ima` file, where purple indicates no flag and green highlights pixels flagged as a cosmic ray by `calwf3` during the “up-the-ramp” fit. [NOTE ADDED IN PROOF: Red points in the right panel were updated with the publication of the Addendum, after discovery of a binning error in the originally published ISR.]*

We noticed a large number of pixels flagged as a CRHIT in this exposure, which was observed using SPARS25 sample sequence, the same sample sequence shown in Figure 1. We repeat the analysis in Figure 10 for stars in Quadrants (Quads) 1 and 4, which comprise the top half of the IR detector. We find that the quad-based non-linearity correction is significantly worse in Quad 1 with deviations up to $\sim 8\%$, compared to Quad 4 with deviations

up to $\sim 5\%$. This strongly implies that the larger number of CR flags in Quad 1 is related to errors in the quadrant-based linearity solution.

This exposure also has $\sim 15\%$ more CRHIT flags identified by `calwf3` than that of the NGC 1851 exposure in Figure 9. This is most likely related to the different sample sequence of the two exposures. The NGC 1851 exposure in the previous section was observed in **STEP100** (linearly spaced readouts early in the ramps ending with logarithmically spaced readouts) while the 47 Tucanae exposure is observed in **SPARS25** (evenly spaced readouts). The smaller spacing between 47 Tucanae reads may cause `calwf3` to erroneously detect pixels as a CRHIT more often compared to a larger time step between reads. We compare the total number of CR flagged peak pixels of sources in Quadrants 1 and 4 in the 47 Tucanae exposures with the two corrections and find that there is a 20% reduction in the number of peak pixels being flagged as CRHIT when using the new correction compared to the current one, while the number of CRHIT flags in Quadrant 4 did not change significantly.

Staring Mode Observations of Standard Star P330E

High signal-to-noise observations of spectrophotometric standard stars serve as an excellent monitor of the IR channels' throughput and stability. P330E is a G-type CALSPEC standard star used for flux calibration monitoring due to its well-characterized spectral energy distribution. We reprocess P330E observations across three filters (F110W, F140W, and F160W) from past WFC3 photometric monitoring programs spanning from cycles 17 - 30 (2009 - 2022) to test our new linearity correction file. All observations are taken with RAPID sample sequence with a mix of small subarray apertures to avoid saturation, while still providing a large number of reads to obtain an accurate ramp fit. Ramps with four or fewer reads are removed from our analysis. Table 2 in the Appendix lists the Proposal ID, filter, sub-array, aperture used, exposure time (s), and rootnames of the P330E exposures.

Figure 11 shows the instantaneous count rate (e^-/s) versus the fluence level (e^-) for the peak pixel value as determined by `hst1pass` of one P330E exposure `ie7h20bvq` in F110W corrected with the current and new correction file. This exposure was acquired with the RAPID sample sequence using the **IRSUB64** subarray in order to acquire a large number of reads (**NSAMP** = 8) in the short 0.4-second exposure before the star saturates. In the image, the star was positioned at the center of a pixel and therefore reaches the saturation limit of the pixel, whereas other images of this star do not get close to the full well limit due to the star being centered at the corner of four pixels and the flux of the peak pixel is spread out. The error bars represent the propagated uncertainties of the instantaneous count rates derived from the **ERR** extensions of the `ima` reads. At later `ima` reads, where the fluence level is close to saturation, the new correction (blue) brings the count rates of the higher ramps closer to linearity with the earlier ramps compared to the current correction (orange). Most notable is a $\sim 3\%$ improvement in the last read before saturation begins compared to the measured **flt** count rate, validating the improvements with the new pixel-based solution.

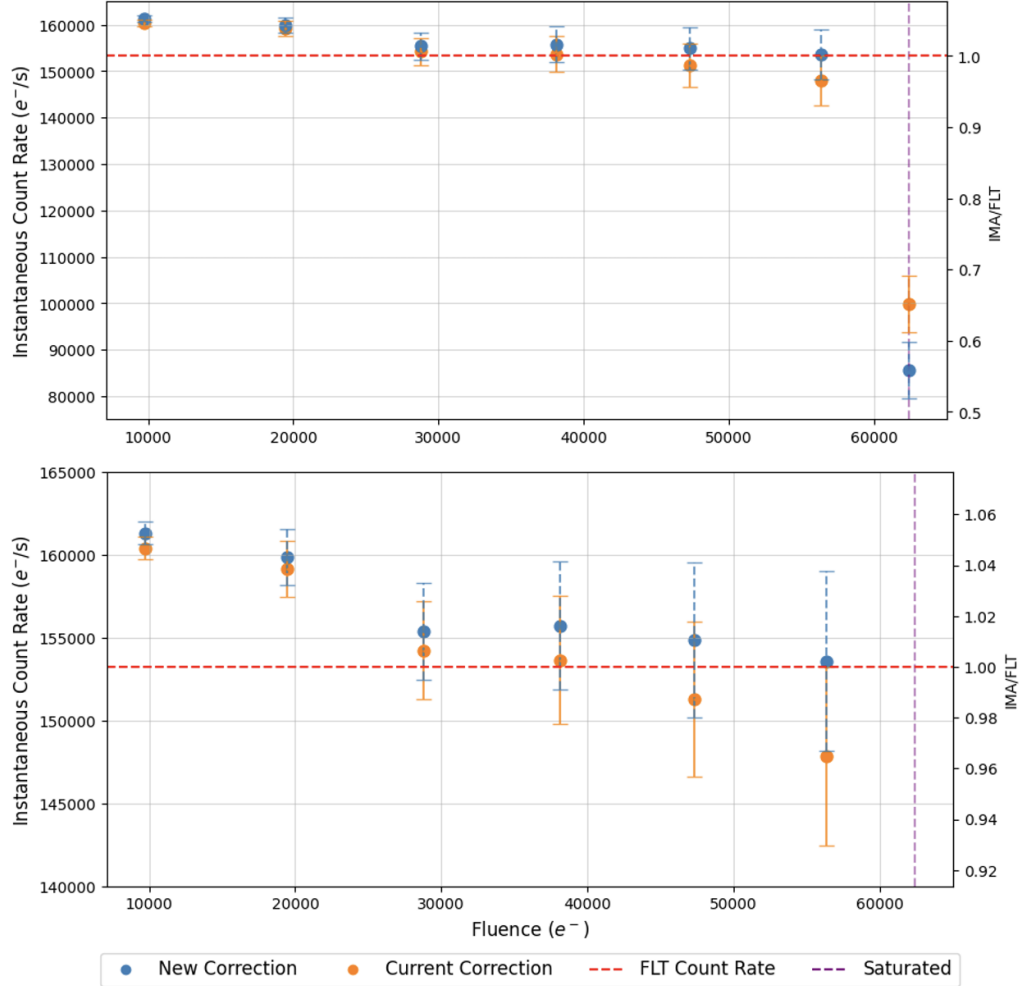


Figure 11: Instantaneous count rate (e^-/s) versus the fluence level (e^-) for the peak pixel value in F110W P330E exposure `ie7h20bvq` corrected with the new non-linearity correction file (blue) and the current (2009) correction file in the pipeline (orange). The count rate measured in the `flt` file (red dotted line) and the fluence level at which saturation is first flagged in the `DQ` array (purple dotted line) is also shown. The error bars represent the propagated uncertainties of the instantaneous count rates derived from the `ERR` extensions of the `ima` reads. At ramps approaching saturation, the new correction improves the linearity compared to the current correction, most notably a $\sim 3\%$ improvement in the last ramp before saturation begins at a fluence level of $\sim 55,000 e^-$. The bottom panel is identical to the top except for a smaller y-axis range.

Furthermore, we repeat a similar analysis to that conducted on the INTFLAT observations in the earlier section. We measure the ratio between the instantaneous count rate between `ima` reads and the `flt` count rate, as well as the fluence level at the peak pixel coordinate identified by `hst1pass` of P330E only (as opposed to measuring every pixel observed and then calculating the sigma-clipped mean, as we did with the INTFLATs). Figures 12, 13, and 14 show the count rate ratio versus the fluence level for each read of every P330E ramp for F110W, F140W, and F160W, respectively. The median-binned statistic with n

`bins = 10` is also plotted. Points are colored based on their DQ flags in the `ima` extension, where purple = no flags, dark blue = saturated pixel, light green = CR flag, and yellow = both saturated and CR flag.

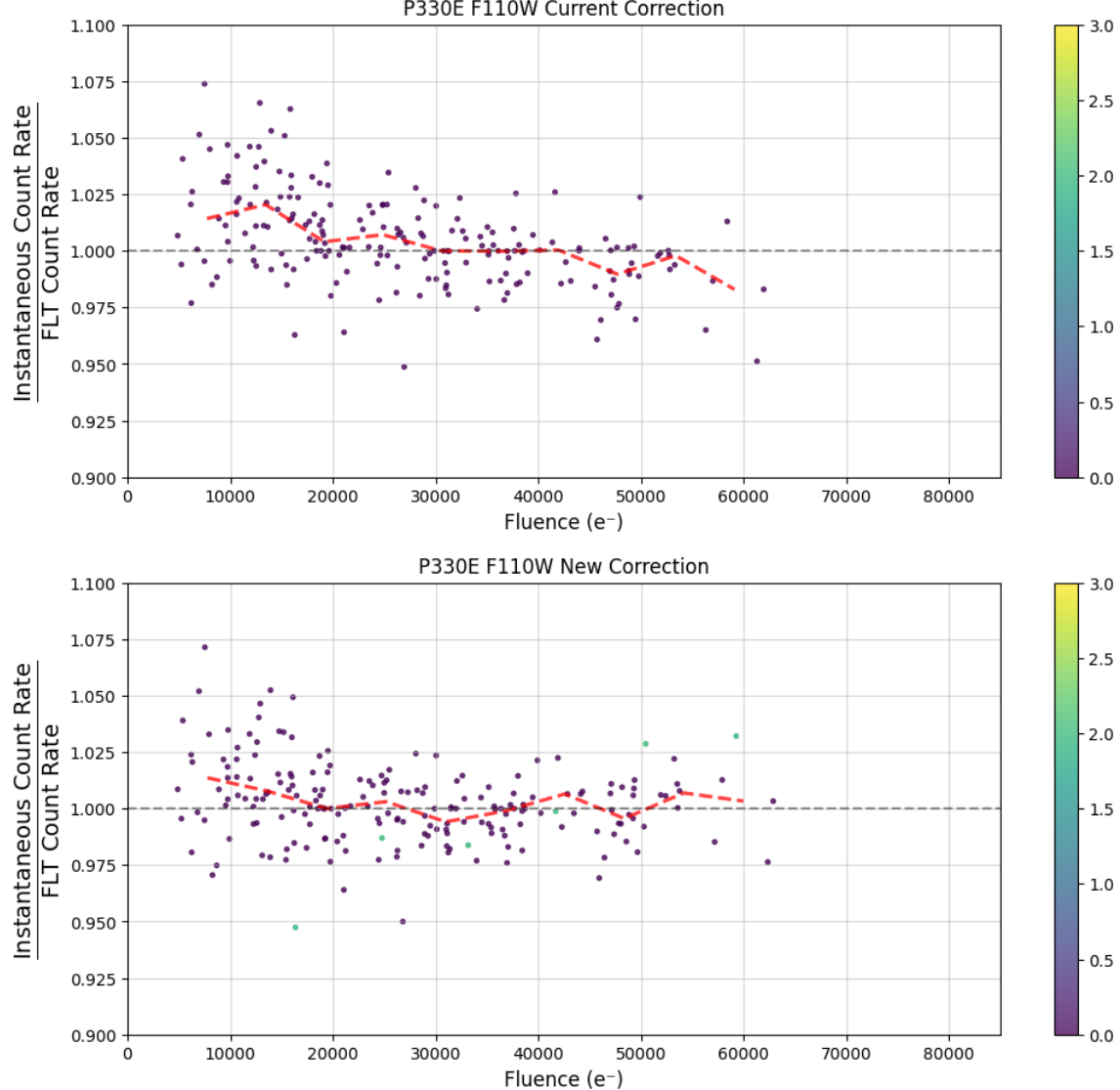


Figure 12: *Ratio of the instantaneous count rate of `ima` reads and the `flt` count rate versus the fluence level (e^-) for P330E observations taken in F110W with the current (2009) linearity correction (top) and the new linearity correction (bottom). The colorbar presents the DQ flags of the pixel: purple ($value = 0$) = no flags, dark blue (1) = saturated pixel, light green (2) = CR flag, and yellow (3) = both saturated and CR flag. The median-binned statistic (red dashed line) is overplotted, and a horizontal line at a count rate ratio of 1.0 represents near-perfect linearity. The new correction file improves the linearity of P330E count rate measurements by $\sim 2\%$ at higher fluence levels in F110W.*

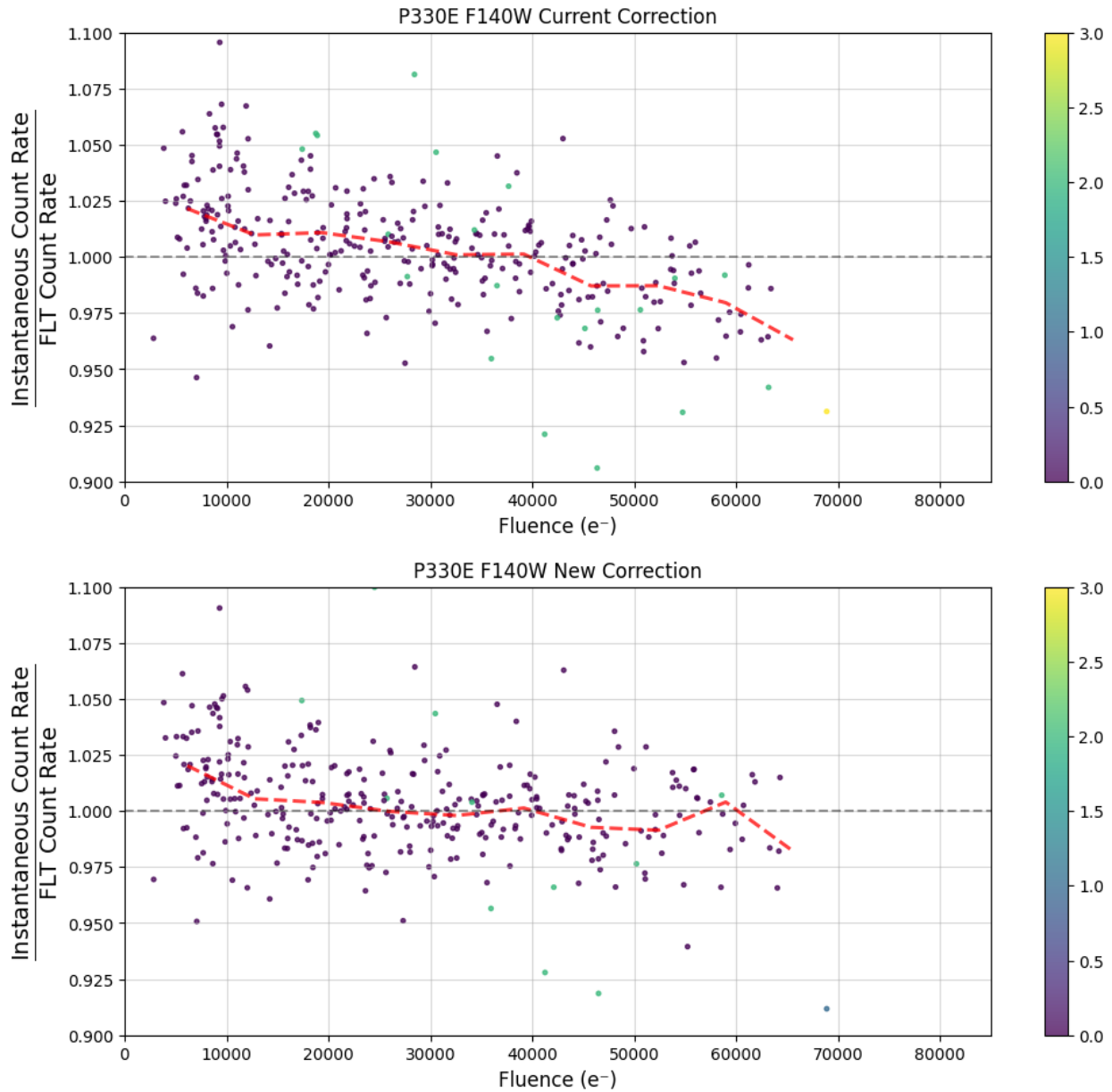


Figure 13: Same as Figure 12, but for F140W. The new correction file improves the linearity of P330E count rate measurements by $\sim 2\%$ at higher fluence levels in F140W.

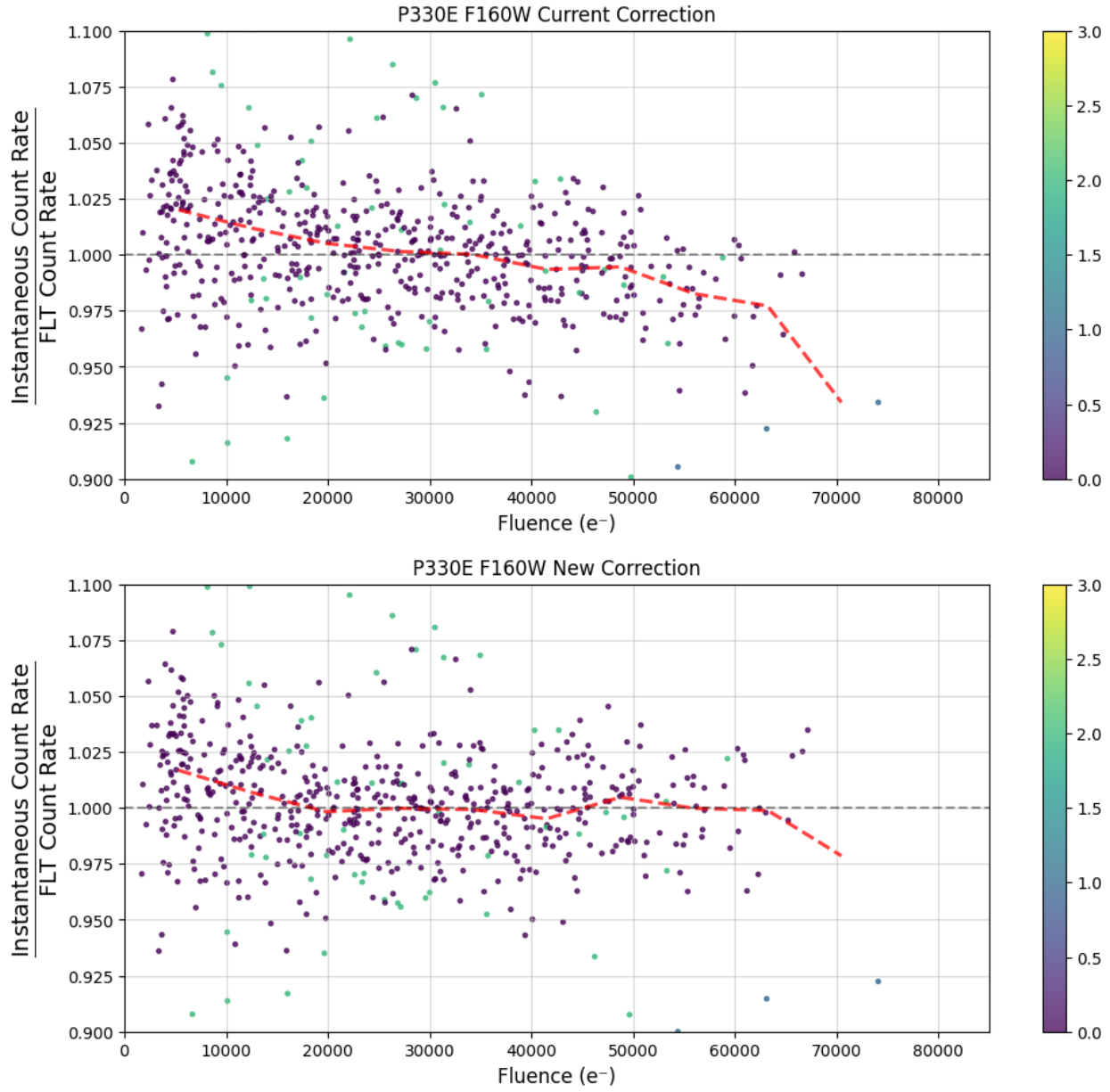


Figure 14: Same as Figure 12, but for F160W. The new correction file improves the linearity of P330E count rate measurements by $\sim 4\%$ at higher fluence levels in F160W.

In all three filters tested, the new correction file improves the linearity, especially at the bright end. At higher fluence levels, the new correction shows the count rate ratio approaches 1.0—indicating near-perfect linearity—by 2–4% more than the current correction across all three filters, with the most significant improvement of 4% in F160W.

Grism Observations of CALSPEC Standard Stars

P330E

IR grism observations of P330E (G102 and G141) were reprocessed with the current and new non-linearity corrections (Bohlin 2025, private communication) using the methodology described in Bohlin and Deustua (2019). These grism observations are part of the WFC3/CAL IR Grism Flux Monitor and were recently used to measure the time-dependent sensitivity of the IR detector (Som et al. 2024). Table 3 in the Appendix lists the proposal ID, rootname, grism filter, and exposure time for the observations used.

Figures 15 and 16 show the relative sensitivity over time based on P330E observations in G102 and G141 with the current and new non-linearity correction, respectively. The points are color coded by their exposure time. In G102, we see an improvement in the scatter (~ 0.001 improvement in the RMS when using the new correction) among observations during the same visit in the 2012 series, where the exposure (500 sec) was closer to saturation than in other exposures. This is consistent with previous tests showing that the correction improves the linearity of the count rate close to the saturation limit.

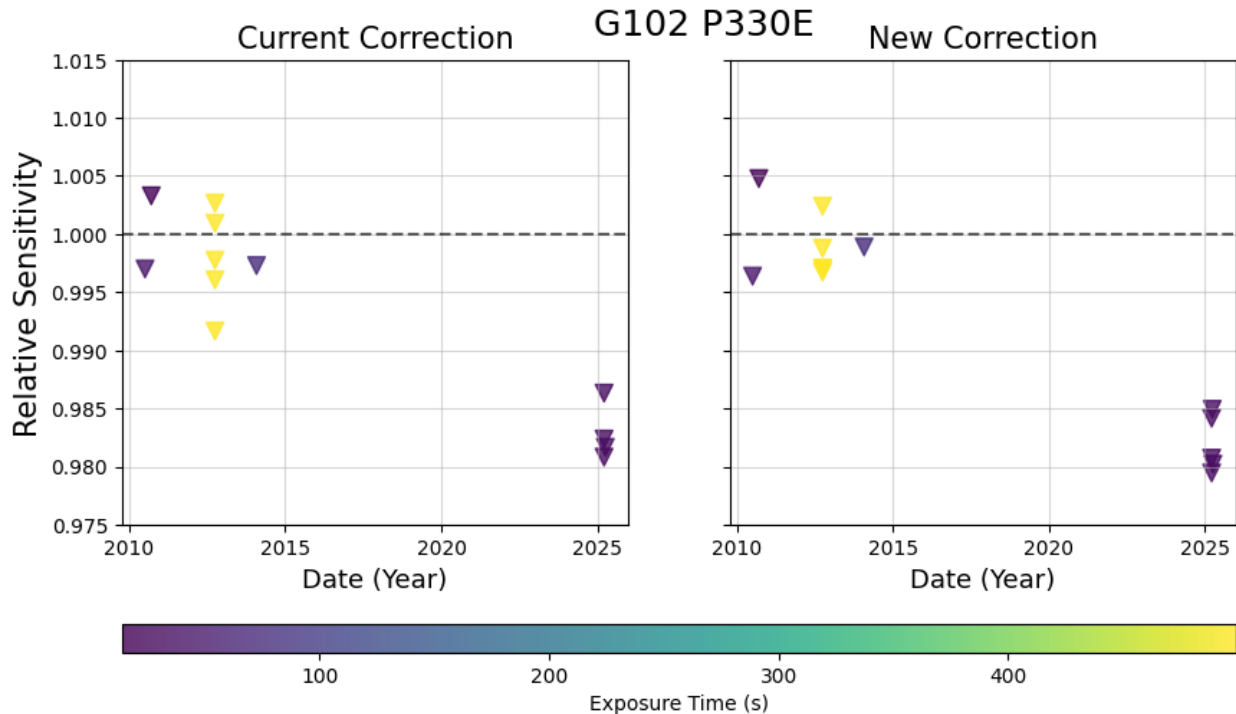


Figure 15: *Relative sensitivity versus date for G102 observations of P330E calibrated with the current (2009; left) and new (right) non-linearity correction. Points are colored based on their exposure time. There is an improvement in the scatter for yellow points in ~ 2012 , where the long 500-second exposures taken with the STEP50 sample sequence are closer to full well saturation than other visits. Purple points denote observations in a variety of sample sequences and exposure times ranging from 14 to 73 seconds.*

However, for G141, the correction does not improve the linearity of the count rates for the 2012 visit, and the results actually have larger scatter. This visit in particular is affected by self-induced persistence to a greater degree than other visits, and its results may be inconclusive. However, the change between the two corrections in all G141 observations (including the one affected by persistence) is negligible ($< 0.1\%$).

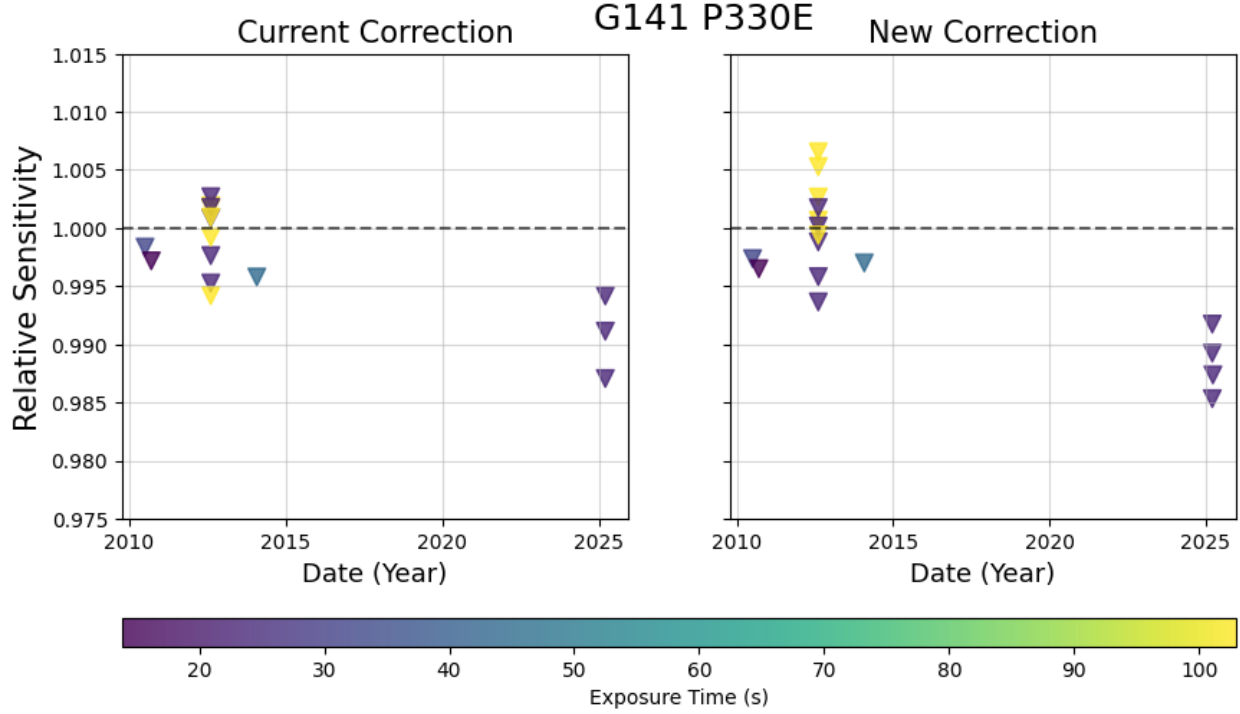


Figure 16: *Same as Figure 15, but for G141. While there is no significant improvement in the scatter for a given visit, the new correction increases the brightness of the yellow points (103 seconds, SPARS10) by $\sim 0.5\%$. These data are affected by self-persistence from prior exposures in purple (23 sec, RAPID) due to a lack of dithering between pairs of long and short observations.*

GD71

To test the spatial dependence of the linearity calibration, dithered observations of the CALSPEC standard star GD71 acquired in the G102 and G141 grisms were reprocessed with the new linearity solution (Bohlin 2025, private communication). These observations are part of the IR grism flux monitor calibration program and have recently been used to measure sensitivity losses of the IR detector as a function of wavelength (Som et al. 2024). For observations acquired on the same date (but on different regions of the detector), the large (1-2%) scatter in photometry was originally attributed to errors in the flat field. Table 4 in the Appendix lists the rootname for the set of dithered GD71 observations acquired in 2015, with a single visit for each IR grism.

Figure 17 plots the (X,Y) position of the dithered exposures taken in each visit. Observa-

tions calibrated with the current (circle) and new (triangle) linearity corrections are colored by their normalized sensitivity to the value at the reference position near the center of the detector. Results from data processed with the new correction are offset by 30 pixels along the X-axis to help compare the difference between the two non-linearity corrections.

The sensitivity of GD71 in both filters, when calibrated with both correction reference files, is nearly identical at all parts of the detector measured. We would expect the sensitivity to improve on the left edge of the detector with the new correction, as the current correction has an abnormality where it flags pixels as CRHIT more often due to the saturated flats used in the derivation of the current correction (see Figure 1). However, we see a negligible change in sensitivity, indicating that the left edge of the detector may still experience the same non-linearity issues with the new pixel-based correction. In addition, it is important to note that there is no evidence of the non-linearity becoming worse with the new correction.

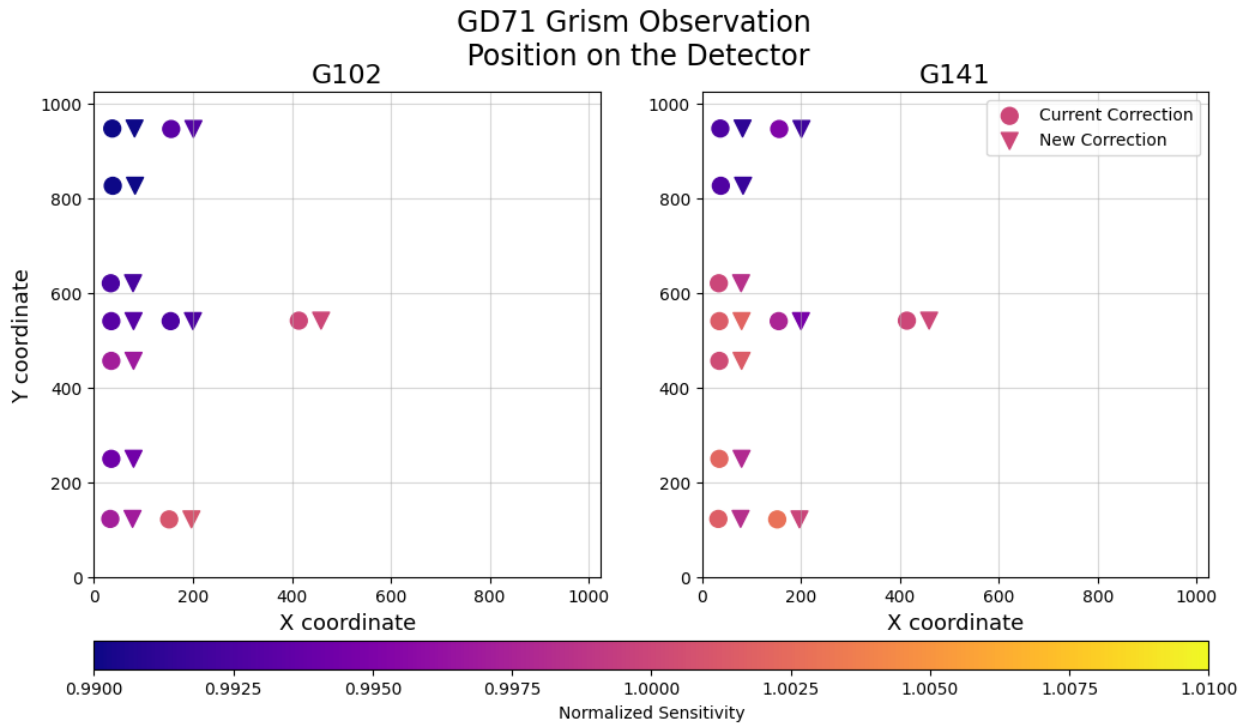


Figure 17: (X, Y) coordinate of GD71 taken in with *SPARS25* sample sequence for dithered exposures of G102 and G141 calibrated with the current (2009; circle) and new (triangle) non-linearity correction files. Points are colored based on their sensitivity, normalized to an image at the IR grism reference position near the center of the detector. Results from data processed with the new correction are shifted by 30 pixels along the X-axis to help compare differences with the previous correction. In general, the count rates are not significantly different between the old and new linearity corrections. The upper left corner of Quad 1 has lower observed count rates compared to the center of the detector, even with the new linearity correction.

IR Zeropoints

In late 2024, the first set of time-dependent WFC3/IR inverse sensitivities (zeropoints) was delivered to the HST Calibration Reference Data System (CRDS) (Calamida et al. 2024) and installed in the automated calibration pipeline. These zeropoints are important for users to obtain accurate photometry, as WFC3/IR has experienced a 1–2% total decline in photometric sensitivity (depending on filter) since installation in 2009 (Marinelli et al. 2024). In this section, we present relative photometry from `flt` files of staring mode observations spanning July 2009 to August 2025 for the CALSPEC standards used in Calamida et al. (2024).³ We address how the updated linearity solution affects this photometry to determine if the IR zeropoints should be recalculated and redelivered.

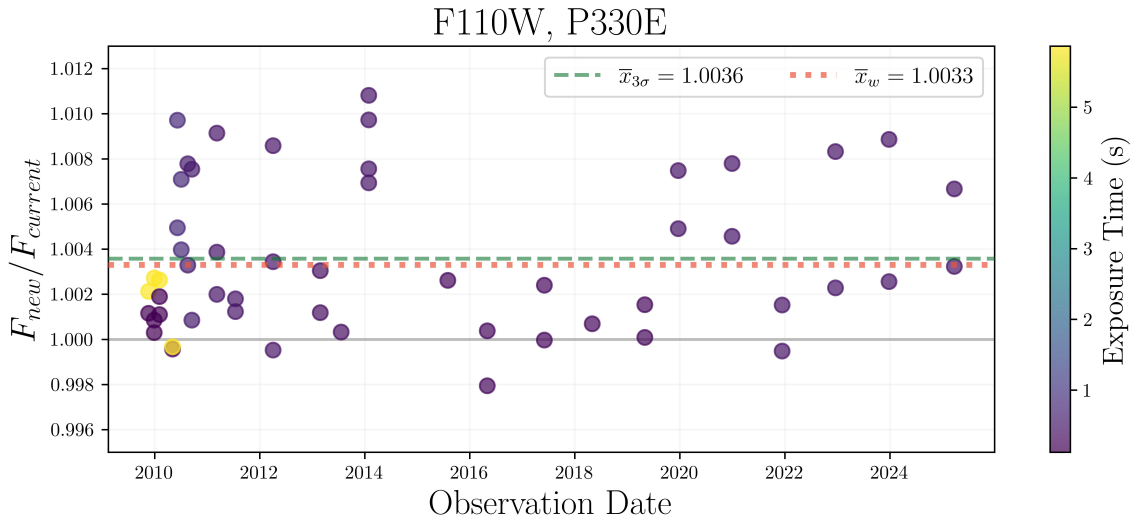


Figure 18: *Flux ratios as a function of time for `flt` observations of P330E in the F110W filter, comparing the measured flux (e^-/s) after implementing the new linearity solution (F_{new}) to the flux using the current (2009) calibration ($F_{current}$). Points are colored by exposure time (s), the 3σ -clipped mean is a green dashed line, and the mean flux ratio (weighted by photometric errors) is a pink dotted line.*

To test the impact of the linearity solution, we recalibrated all observations of the CALSPEC standards using both the new and current linearity solutions. In Figure 18, we show the effects of the linearity solution on 3-pixel aperture photometry for P330E in the F110W filter. We take the observed count rate from exposures calibrated with the new linearity solution (F_{new}) and divide by the observed count rate of the data calibrated with the current linearity file ($F_{current}$). The resulting ratio ($F_{new}/F_{current}$) is plotted as a function of observation date, and color-coded according to the observation exposure time. A solid line is plotted at 1.0, indicating no change in the count rates between the new and current linearity solutions. Generally, photometry on files calibrated with the new linearity solution yields

³G191B2B, GD-153, GD-71, GRW70, and P330E.

higher measured count rates than photometry of files using the current calibration. We over-plot two statistics to illustrate the behavior of this subset: the 3σ -clipped mean ($\bar{x}_{3\sigma}$) and the weighted mean (\bar{x}_w ; weighted by photometric error). For this target/filter combination, the 3σ -clipped mean and weighted agree within 0.03%, and are both $\approx 0.35\%$ above unity.

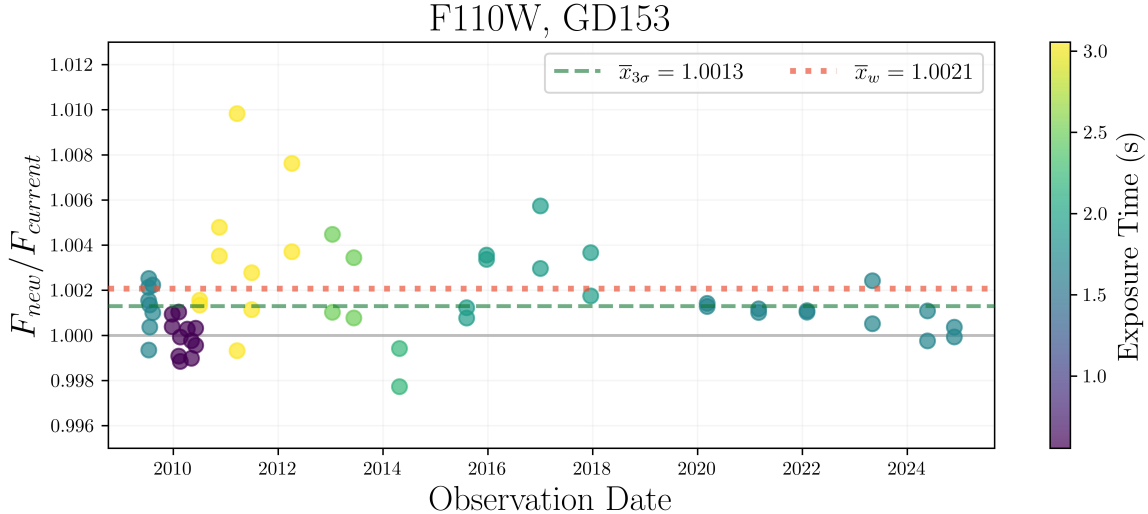


Figure 19: *Same as Figure 18, but for GD-153.*

Figure 19 also plots F110W flux ratios as a function of observation date, but for GD-153. While calibrating the staring mode exposures with the new linearity solution results in slightly higher photometric counts than the current calibration, the increase in observed count rate for this star is less than that observed for P330E in Figure 18. We find the 3σ -clipped mean to be $\approx 0.1\%$ and the weighted mean at $\approx 0.2\%$, underscoring an important detail. Sigma-clipping a sample removes outliers, and in this case, produces a more robust estimation of the mean flux ratio within the distribution of flux ratios. Because \bar{x}_w is weighted by the photometric errors, it better captures the precision of the underlying data.

Following the same process as in Figures 18 and 19, we calculate the flux ratio $F_{new}/F_{current}$ for all observations. Filter/target combinations with a sample size less than five were excluded from further analysis. In the top subplot of Figure 20, we plot the target-and-filter-specific weighted mean as a function of filter pivot wavelength. G191B2B mean ratios are plotted as yellow downward-triangles, GD-153 as red diamonds, GD71 as blue squares, GRW70 as black circles, and P330E as green right-facing triangles. Therefore, the pink dotted line from Figure 18 corresponds to the green triangle at (1153.4, 1.0033), and the same line in Figure 19 matches the red diamond at (1153.4, 1.0021). A line is drawn at 1.0, which, as in Figures 18 and 19, would indicate perfect agreement between the photometry using the new linearity solution and photometry using the current calibration. Notably, all points are above this line: for all target/filter combinations, using the new linearity file results in higher count rates than the current linearity solution.

Within each filter, we then pooled the flux ratios for all stars and calculated the weighted mean (weighted by photometric errors); results are shown in the bottom subplot of Figure

20. The filter-dependent weighted means are plotted as a function of pivot wavelength, and are represented by teal circles. Asymmetric error bars on those points indicate the median absolute deviation as calculated for values above and below the weighted mean. As in Figures 18 and 19, we plot a line at 1.0, and draw the overall weighted mean of all targets and stars (\bar{x}_w) as a horizontal pink dotted line.

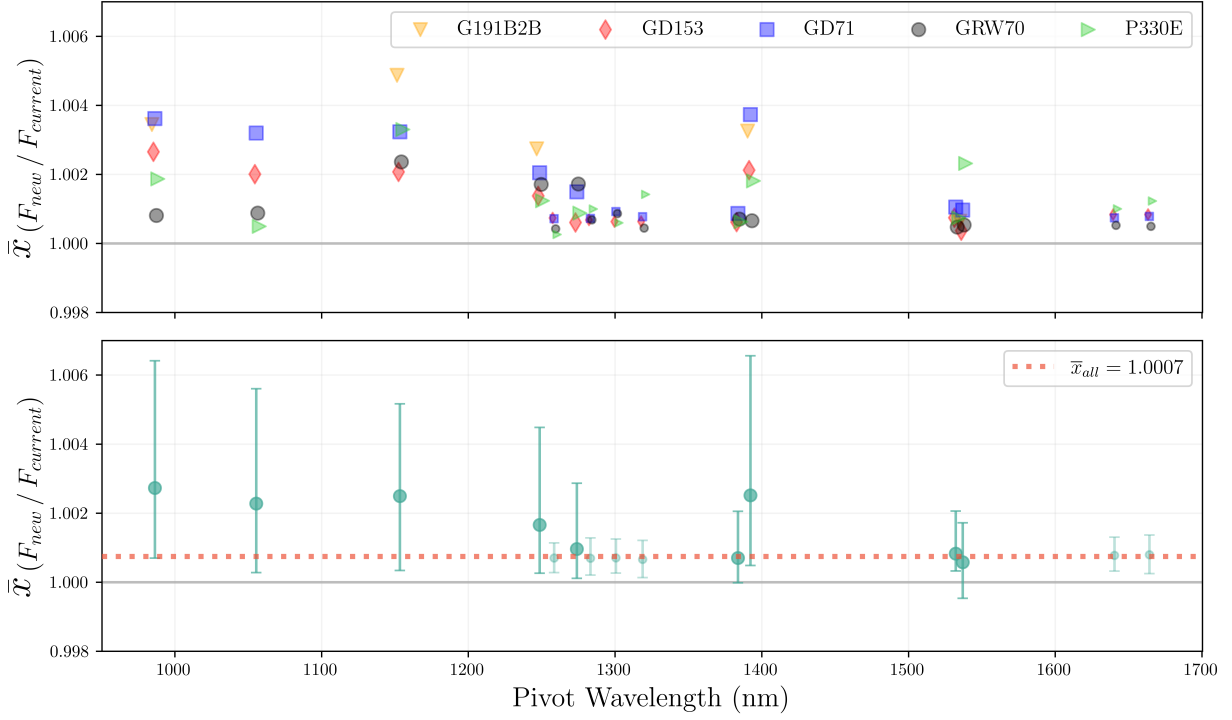


Figure 20: *Mean flux ratios (observed count rates for `flt` data calibrated with the new linearity solution, divided by the observed count rates for the current (2009) solution), weighed by photometric errors, as a function of filter pivot wavelength. Narrow filters are indicated with a smaller marker size. Top: Mean flux ratio per target/filter combination. Bottom: Mean flux ratio for all stars within each filter. Error bars show the median absolute deviation above and below the mean.*

Overall, calibrating with the new linearity solution increases the observed count rate. On a per-star, per-filter basis, as shown in the top subplot of Figure 20, the increase ranges from ~ 0.05 – 0.5% , and can be sensitive to sample size effects. For example, there are only nine F110W exposures of G191B2B, yielding a weighted mean flux ratio of $\sim 0.5\%$. When data from all targets are pooled together, the weighted means of the flux ratios (teal points in the bottom subplot of Figure 20) appear somewhat correlated with filter: bluer filters demonstrate a 0.2 – 0.3% change, but in the reddest filters and all narrow-band filters, the offset is $< 0.1\%$. These data may be influenced by underlying factors such as the shape of the point spread function (PSF) and the width of the filter bandpass.

PSFs in bluer filters are sharper, making the central pixel more likely to hit fluences in the regime ($> 50,000e^-$) for which the current linearity solution performs most poorly. In

that case, the new linearity solution would have a more significant effect on the photometry, thereby driving the mean flux ratio up.

By definition, narrow-band filters transmit only a narrow band of wavelengths. The current linearity solution is most problematic at high fluence levels. When the accumulated signal in a given exposure does not approach saturation, the non-linear response should already be reasonably well-corrected by the current `NLINFILE`. Therefore, while the new linearity solution tends to increase measured source brightness, the effect is lessened at the lower fluence levels that are characteristic of the narrow-band observations taken during WFC3 calibration programs.

Overall, these data indicate only a $\sim 0.1\%$ increase in the total flux (in electrons) for photometry in a 3-pixel aperture for exposures calibrated with the new linearity solution. The RMS variations in the time-dependent IR zeropoints (Calamida et al. 2024) were $\approx 0.5\%$. As such, we deem the image photometry reference file (`IMPHTTAB`) and filter curves⁴ available in CRDS and in use in the automated calibration pipeline are still valid and thus can be used with the new `NLINFILE` for absolute photometry. At this time, new IR zeropoints do not need to be delivered.

Conclusion

The current (2009) linearity reference file provides a quadrant-based average polynomial fit to the IR non-linearity. Using a new pixel-based non-linearity correction developed by Shenoy et al. (2025), we test the improvements in recalibrated data for a variety of targets and observing modes, including: internal flat fields, star clusters, imaging, and grism observation of spectrophotometric standard stars used to define the IR zeropoints. **In general, the new pixel-based correction improves linearity at fluence levels above 50,000 e^- (approximately 2/3 of the full well saturation limit), with improvements up to 7% at the end of the ramp of the `ima` file for pixels reaching the highest fluence level near 80,000 e^- . For 3-pixel aperture photometry in `f1t` images, the typical improvement in photometry is $\sim 0.5\%$, where the new solution makes the observed photometry brighter.**

Our individual findings for the various test datasets can be summarized as follows:

1. Internal Flat Fields: We reprocess internal flat field observations taken with five sample sequence modes which target a range of fluence levels: `SPARS50`, `SPARS25`, `SPARS10`, `STEP25`, and `RAPID`. We find the most considerable improvement in `SPARS25` exposures, where the current non-linearity correction file flags nearly three times as many pixels during the ramp fit (and twice as many pixels for the `SPARS50` exposure) compared to the new correction. We compute the ratio of the `ima` instantaneous count rate and `f1t` average count rate as a function of the fluence level (e^-) for all internal flat fields in the five sample sequences. We find $\sim 0.4\text{--}5\%$ improvements in the peak-to-peak range over

⁴Current WFC3/IR filter curves: `wfc3_ir_F????_008_syn.fits`

all fluence levels in all sample sequence modes, with the most significant improvement in the **SPARS25** flats used to compute the coefficients. These results indicate that the new correction decreases the non-linearity across all fluence levels and for a variety of sample sequences.

2. Star Clusters: We compare the count rates in deep exposures of uncrowded regions in two star clusters taken in different sample sequences: NGC 1851 in **STEP100** and 47 Tucanae in **SPARS25**. Exposures with many reads (**NSAMP**=16) were selected to assess changes in the count rate over a range of fluence levels. For NGC 1851, we find that the new correction improves the linearity of a star’s peak pixel value by 1–2% at fluence levels close to saturation. We find a larger improvement of 5% in the linearity of the peak pixel for stars in 47 Tucanae at high fluence levels. Additionally, we find that the **SPARS25** exposure of 47 Tucanae has a substantially higher fraction of CRHIT flags (**DQ**=8192) compared to the **STEP100** exposure of NGC 1851. This suggests that the current 4-sigma rejection threshold used by **calwf3** to identify cosmic rays during the ramp fitting step may not be appropriate for every sample sequence.
3. Imaging Observations of the G-type Standard Star P330E: We compare a P330E exposure taken in F110W with both linearity correction applied and find that there is a $\sim 3\%$ improvement in the linearity of instantaneous count rates in the last reads before saturation begins with the new pixel-based correction. We analyzed every P330E star-ing mode exposure in our dataset across three different filters: F110W, F140W, and F160W. We find that in all three filters, the new non-linearity correction file improves the linearity of instantaneous reads at high fluence levels by 2–4%, with the largest improvement in the F160W exposures.
4. Grism Observations: We compare G102 and G141 grism observations of P330E calibrated with both non-linearity correction files. We find that the scatter in the relative sensitivity of P330E in the visit with the highest exposure time (500 seconds) is reduced in G102 with the new correction. We see the opposite effect in G141; however, this is due to the self-induced persistence in the exposures.
5. Grism Observation of White Dwarf Standard Star GD71: We plot the (X,Y) position of GD71 observed in grism exposures calibrated with the current and new non-linearity corrections. We compare their normalized sensitivity and find that both corrections return nearly identical normalized sensitivity as a function of position on the detector.

The up-the-ramp fitting step in **calwf3** uses a 4σ rejection threshold to identify cosmic ray hits for an individual pixel. This is accomplished by looking for significant deviations from the average in the instantaneous count rates between reads. With the errors in the current linearity file, this results in overly aggressive flagging (as the resulting changes to instantaneous count rates are detected as CRs), where Quadrant 1 (upper left region of the detector) is more susceptible to spurious CR flagging. While an improvement in photometry is found for all sample sequences, we find that the CR-flagging behavior appears to be related to the sample sequence that was used to acquire the data. For example, **SPARS** sequences (reads evenly spaced in time) tend to show CR flags populated in early reads of the exposure,

whereas STEP sequences (reads evenly spaced early in ramps, then logarithmically spaced later in ramps) tend to have CR flags populated in later reads as the signal approaches full well. By significantly reducing the number of erroneous CR flags, the total signal used in WFC3/IR ramp fits increases, leading to more precise count rates in the calibrated exposures when using the new correction.

Finally, we use the new linearity correction to recalibrate all observations of CALSPEC standards used by Calamida et al. (2024) to quantify any changes to the latest published IR zeropoints. We find that the new solution increases the observed count rate by up to $\sim 0.5\%$ for F110W observations of G191B2B, for example. However, the weighted average change for all stars in a given filter is only $\sim 0.2\%$ for bluer filters and $\sim 0.1\%$ for redder filters and for all narrow-band filters. These changes are smaller than the RMS variations in the published WFC3 zeropoints ($\sim 0.5\%$). This suggests that the current image photometry reference file (`IMPHTTAB`) can still be used together with the new `NLINFILE` reference file for absolute photometry.

The pixel-based `NLINFILE 9au15283i.lin.fits` was delivered to CRDS and the automated calibration pipeline in October 2025, replacing the 2009 quad-based correction. This reference file was then superseded by the February 2026 delivery of `a2412448i.lin.fits`, incorporating small improvements to the polynomial coefficients discussed in the Addendum below. Because the latest non-linearity correction affects the observed count rates, we advise users to retrieve updated data products from MAST after all IR data has been reprocessed with `calwf3` in Spring 2026.

Recommendations

CR flags are populated in the DQ array of the `ima` file and are not propagated into the DQ array of the `f1t` data. These flags can be a useful diagnostic of an error in `calwf3`'s up-the-ramp fit, and we recommend that users compare the SCI and DQ arrays of the `ima` file to help determine whether the flux in that pixel is reliable in the calibrated `f1t` file. DQ array values ≥ 8192 , which coincide with the position of sources in the SCI array or in a particular IR quadrant, can indicate that the ramp fit in `calwf3` may be inaccurate, affecting the count rates in the `f1t` data products. While the new linearity solution reduces the number of CR flags at high fluence levels, it does not fully resolve CR-flagging issues at the beginning of the ramp, which are more prevalent in `SPARS` (versus `STEP`) sample sequences.

In general, the new linearity solution significantly reduces non-linearity response of the IR detector. However, the correction still shows 1-2% deviations from a flat ramp at high fluence levels for some sample sequences (see Figures 2–6). For this reason, we recommend comparing count rates between the `ima` and `f1t` data products. For sources with fluence levels exceeding $\sim 2/3$ the full well limit ($\sim 50,000 e^-$), the `f1t` photometry may be fainter than in the cumulative read of the `ima` file ([SCI,1] extension), even with the new linearity correction. Saturation maps are provided in the NODE extension of the new `NLINFILE` reference file in units of DN. To convert to electrons, multiply by the mean IR gain of $2.25 e^-/DN$ (Gosmeyer and Baggett 2015).

Finally, in some cases, users may wish to mask the last read(s) before sources of interest saturate in long exposures and reprocess the data with `calwf3` to generate an improved `flt` file for photometry of bright sources. The process for rejecting reads is described in the following [WFC3 Jupyter Notebook](#).

Acknowledgments

The authors would like to thank Benjamin Kuhn, Joel Green, and Sylvia Baggett for their insightful review of this report. We also like to thank Ralph Bohlin for his expertise and analysis on the IR grism observations of CALSPEC standard stars.

References

Anderson, J. (July 2022). *One-Pass HST Photometry with hst1pass*. Instrument Science Report WFC3 2022-5, 55 pages.

Bajaj, V. et al. (Oct. 2022). *WFC3/IR Photometric Stability Stellar Cluster Study*. WFC3 Instrument Science Report 2022-07, 28 pages.

Bohlin, Ralph C. and Susana E. Deustua (June 2019). “CALSPEC: Wide Field Camera 3 Infrared Grism Spectrophotometry”. In: *Astronomical Journal* 157.6, 229, p. 229. DOI: [10.3847/1538-3881/ab1b50](https://doi.org/10.3847/1538-3881/ab1b50).

Calamida, Annalisa et al. (Dec. 2024). *New Time-Dependent WFC3/IR Inverse Sensitivities*. Instrument Science Report WFC3 2024-13, 22 pages.

Canipe, Alicia, Massimo Robberto, and Bryan Hilbert (2017). *A New Non-Linearity Correction Method for NIRCam*. Tech. rep. Technical Report JWST-STScI-005167. STScI.

Gosmeyer, C. M. and S. Baggett (Sept. 2015). *WFC3 IR Gain from 2010-2015*. Instrument Science Report WFC3 2015-14, 26 pages.

Hilbert, B. (Jan. 2008). *WFC3 TV3 Testing: IR Channel Nonlinearity Correction*. Instrument Science Report WFC3 2008-39, 14 pages.

— (July 2014). *Updated non-linearity calibration method for WFC3/IR*. Instrument Science Report WFC3 2014-17, 32 pages.

Long, Knox S. et al. (Nov. 2010). *WFC3/IR Persistence as Measured in Cycle 17 using Tungsten Lamp Exposures*. WFC3 Instrument Science Report 2010-17, 12 pages.

Marinelli, Mariarosa et al. (May 2024). *Time-Dependent Sensitivity of the WFC3/IR Detector*. Instrument Science Report WFC3 2024-06, 56 pages.

Pagul, Amanda and Isabel Rivera (2024). “WFC3 Data Handbook v. 6”. In: *WFC3 Data Handbook v. 6*. Vol. 6, p. 6.

Shenoy, Sachindev S. et al. (Oct. 2025). *Pixel-Based Non-Linearity Correction for the WFC3 IR Detector*. WFC3 Instrument Science Report 2025-08.

Som, D. et al. (Mar. 2024). *Sensitivity Evolution of WFC3/IR Using Spatial Scanning Photometry and Grism Spectrophotometry*. Instrument Science Report WFC3 2024-01, 12 pages.

Appendix

Table 1: *Sample sequence, nsamp, exposure time, rootnames, and proposal ID for internal flat field observations used to validate the new linearity correction. All exposures are part of the IR linearity monitoring program taken every year. Sample sequence patterns are listed in the [HST Phase II Proposal Instruction Handbook](#).*

Samp_Seq	n samp	Exptime (s)	Rootname	Proposal ID
SPARS25	16	313.122345	ibmg18gsq, ibmg17s8q, ibmg08vbq, ibmg09h7q ibmg01iwq, ibmg16rcq, ibmg15qqq, ibmg14q6q, ibmg13gvq, ibmg12z9q, ibmg10uzq, ibmg11vwq, ibmg07jtq, ibmg06edq, ibmg05dfq, ibmg04chq, ibmg03aaq, ibmg02siq, ic5n08kkq, ic5n07joq, ic5n09mzq	12352 12352 13079
SPARS25	16	352.939514	ic5n04ahq, ic5n05ysq, ic5n06bmq	13079
STEP25	16	274.234863	ic5n01hwq, ic5n02itq, ic5n03hmq	13079
RAPID	16	43.984360	ic5n10faq, icfh06ezq, icfh07goq, icfh08hgq, icfh09r3q, icpo04fzq, icpo05ggq, icpo06e7q, icpo07gsq, id0e04drq, id0e05i1q, id0e06k0q, id0e07ebq, idby04adq, idby05tlq, idby06usq, idby07wcq, idou04d2q, idou05n1q, idou06g7q, idou07hyq, idy704deq, idy705g5q, idy706mnq, idy707lrq, ie0j07q6q, ie0j08qgq, ie0j09qoq, ie0j10qyq, iefv07pnq, iefv08rgq, iefv09dyq, iefv10euq, ielx07t2q, ielx08ucq, ielx09hfq, ielx10oyq, iexl07hcq, iexl08myq, iexl09rsq, iexl10zpq, if4y07kuq, if4y08ciq, if4y09l1q, if4y10mcq, ifcn07fsq, ifcn08ggq, ifcn09kiq, ifcn10q8q	13079 13563 14009 14375 14538 14987 15579 15724 16404 16576 17012 17358 17678
SPARS10	16	142.945755	ibvl06snq, ibvl07vtq, ibvl18v7s, ibvl19v4q	12696
SPARS50	11	452.936035		

Table 2: *Proposal ID, filter, sub-array, exposure times, and rootname for P330E observations used to validate the new linearity correction. All exposures were taken in RAPID sample sequence and had n-samps between 5–15 reads. ie7h20bvq is highlighted as it was used to make Figure 11.*

Proposal ID	Filter	Aperture	Exptime (s)	Rootname
11451	F110W	IRSUB128	0.901640	iaac11gwq, iaac11heq, iaac12tgq, iaac12tyq, iaac13ieq, iaac13iwq, iaac14ymq, iaac14z4q
11451	F140W	IRSUB128	0.901640	iaac14z6q, iaac14yoq, iaac13iyq, iaac13igq, iaac12tiq, iaac11hgq, iaac11gyq, iaac12u0q
11451	F160W	IRSUB128	0.901640	iaac12trq, iaac11h7q, iaac12u9q, iaac13ipq, iaac13j7q, iaac14yxq, iaac14zfq, iaac11hpq
11926	F110W	IRSUB128	0.563525	ibcf60u1q, ibcf60ttq, ibcf61wpq, ibcf61wwq
11926	F110W	IRSUB128	0.788935	ibcf0ai9q, ibcf0aimq, ibcf0aj8q, ibcf0ajgq, ibcf0cuzq, ibcf0cvbq
11926	F140W	IRSUB128	0.788935	ibcf61wyq, ibcf61wrq, ibcf60u3q, ibcf60tvq
11926	F140W	IRSUB128	0.901640	ibcf0ajiq, ibcf0aibq, ibcf0aoioq, ibcf0aj5q, ibcf0cv1q, ibcf0cvdq
11926	F160W	IRSUB128	1.352460	ibcf61wzq, ibcf60u4q, ibcf61wsq, ibcf60twq
11926	F160W	IRSUB128	1.577870	ibcf0ajhq, ibcf0cv3q, ibcf0aj3q, ibcf0aiqq, ibcf0aidq, ibcf0cvfq
11926	F160W	IRSUB64	0.243096	ibcf23rtq, ibcf24oxq, ibcf23s9q, ibcf22grq, ibcf22g9q, ibcf21ynq, ibcf21xgq, ibcf24pdq
12334	F110W	IRSUB128	0.450820	ibnx16h9q, ibnx16h3q, ibnx16gyq, ibnx04dcq, ibnx04d6q, ibnx04d1q
12334	F140W	IRSUB128	0.676230	ibnx16hbq, ibnx16h5q, ibnx04d8q, ibnx04deq, ibnx04d3q, ibnx16h0q
12334	F160W	IRSUB128	1.239755	ibnx16hcq, ibnx16h6q, ibnx16h1q, ibnx04dfq, ibnx04d9q, ibnx04d4q
12699	F110W	IRSUB128	0.450820	ibwi02miq, ibwi02mnq, ibwi02msq
12699	F140W	IRSUB128	0.676230	ibwi02mkq, ibwi02mpq, ibwi02muq
12699	F160W	IRSUB128	1.239755	ibwi02mlq, ibwi02mvq, ibwi02mqq
13089	F140W	IRSUB128	0.676230	ic5s14jrq, ic5s14jjq, ic5s10hjq, ic5s10hbq
13089	F160W	IRSUB128	1.014345	ic5s10hcq, ic5s14jkq, ic5s10hkq, ic5s14jsq
13573	F160W	IRSUB128-FIX	1.577870	icfs12ajq, icfs12akq
13573	F160W	IRSUB256-FIX	3.889411	icfs12alq, icfs12amq

Continued on next page

Table 2 *continued.*

Proposal ID	Filter	Aperture	Exposure Time (s)	Rootname
13575	F110W	IRSUB128	0.450820	ich319ngq, ich319naq, ich319n4q, ich319nmq
13575	F140W	IRSUB128	0.563525	ich319npq, ich319njq, ich319n7q, ich319ndq
13575	F160W	IRSUB128	1.014345	ich319n8q, ich319neq, ich319nkq, ich319nqq
14021	F110W	IRSUB64	0.243096	icrw02eoq, icrw02enq
14021	F140W	IRSUB64	0.425418	icrw02elq, icrw02emq
14021	F160W	IRSUB128	0.901640	icrw02evq, icrw02ewq
14384	F110W	IRSUB64	0.243096	id2402a5q, id2402a4q
14384	F140W	IRSUB128	0.450820	id2402a7q, id2402a6q
14384	F160W	IRSUB128	0.901640	id2402afq, id2402aeq
14883	F110W	IRSUB64	0.243096	iddn09jwq, iddn09jxq
14883	F140W	IRSUB128	0.450820	iddn09jyq, iddn09jzq
14883	F160W	IRSUB128	0.901640	iddn09k6q, iddn09k7q
14992	F110W	IRSUB64	0.243096	idor09n3q, idor09n2q
14992	F140W	IRSUB128	0.450820	idor09n5q, idor09n4q
14992	F160W	IRSUB128	0.901640	idor09ncq, idor09ndq
15582	F110W	IRSUB64	0.243096	idw109oqq, idw109opq
15582	F140W	IRSUB128	0.450820	idw109orq, idw109osq
15582	F160W	IRSUB128	0.901640	idw109ozq, idw109p0q
16030	F110W	IRSUB64	0.425418	ie7h20bvq , ie7h20bwq
16030	F140W	IRSUB128	0.788935	ie7h20bxq, ie7h20byq
16030	F160W	IRSUB128	1.127050	ie7h20c6q, ie7h20c5q
16415	F110W	IRSUB64	0.425418	iege22rlq, iege22rmq
16415	F140W	IRSUB128	0.788935	iege22roq, iege22rnq
16415	F160W	IRSUB128	1.127050	iege22rzq, iege22s0q
16579	F110W	IRSUB64	0.425418	iemg20b7q, iemg20b6q
16579	F140W	IRSUB128	0.788935	iemg20b8q, iemg20b9q
16579	F160W	IRSUB128	1.127050	iemg20bhq, iemg20bgq
17015	F110W	IRSUB64	0.425418	iev520xpq, iev520xoq
17015	F140W	IRSUB128	0.788935	iev520xqq, iev520xrq
17015	F160W	IRSUB128	1.127050	iev520xyq, iev520xzq

Table 3: *Grism, date (year), rootname, proposal IDs, exposure times, and sample sequence of grism observations of P330E used to validate the new linearity correction.*

Grism	Date (Year)	Rootname	Proposal ID	Exptime (s)	Samp_Seq
G102	2010.51	ibcf0cvnq	11926	43.98	RAPID
G102	2010.71	ibcf61xnq	11926	13.83	STEP25
G102	2012.75	ibwib6m8q	12699	499.23	STEP50
G102	2012.75	ibwib6m9q	12699	499.23	STEP50
G102	2012.75	ibwib6mbq	12699	499.23	STEP50
G102	2012.75	ibwib6mdq	12699	499.23	STEP50
G102	2012.75	ibwib6mfq	12699	499.23	STEP50
G102	2014.08	ich319ogq	13575	72.94	SPARS10
G102	2025.21	ifdg04a2q	17681	32.25	RAPID
G102	2025.21	ifdg04a4q	17688	32.25	RAPID
G102	2025.21	ifdg04a7q	17688	32.25	RAPID
G102	2025.23	ifi520f6q	17688	32.25	RAPID
G102	2025.25	ifdg05awq	17688	32.25	RAPID
G141	2010.51	ibcf0cvoq	11926	32.25	RAPID
G141	2010.71	ibcf61xoq	11926	13.83	STEP25
G141	2012.61	ibtwb4bcq	12336	23.45	RAPID
G141	2012.61	ibtwb4bdq	12336	102.94	SPARS10
G141	2012.61	ibtwb4bfq	12336	23.45	RAPID
G141	2012.61	ibtwb4bgq	12336	102.94	SPARS10
G141	2012.61	ibtwb4biq	12336	23.45	RAPID
G141	2012.61	ibtwb4bjq	12336	102.94	SPARS10
G141	2012.61	ibtwb4blq	12336	23.45	RAPID
G141	2012.61	ibtwb4bmq	12336	102.94	SPARS10
G141	2012.61	ibtwb4boq	12336	23.45	RAPID
G141	2012.61	ibtwb4bpq	12336	102.94	SPARS10
G141	2014.08	ich319oeq	13575	43.98	RAPID
G141	2025.21	ifdg04a9q	17688	23.45	RAPID
G141	2025.21	ifdg04acq	17688	23.45	RAPID
G141	2025.21	ifdg04aeq	17688	23.45	RAPID
G141	2025.23	ifi520f4q	17681	23.45	RAPID

Table 4: *Grism filter and rootname for every GD71 exposure used to validate the new linearity correction. All exposures are 103 seconds long, taken in SPARS25, and are a part of WFC3 program 14024. Bolded exposures are the exposure that the data is normalized to in Figure 17.*

Grism	Rootname	Grism	Rootname
G102	icqw01z1q	G141	icqw02h3q
G102	icqw01zjq	G141	icqw02haq
G102	icqw01zrq	G141	icqw02haq
G102	icqw01zvq	G141	icqw02i2q
G102	icqw01zyq	G141	icqw02i5q
G102	icqw01auq	G141	icqw02i9q
G102	icqw01ayq	G141	icqw02icq
G102	icqw01b1q	G141	icqw02igq
G102	icqw01b5q	G141	icqw02ijq
G102	icqw01b9q	G141	icqw02inq
G102	icqw01bcq	G141	icqw02iqq

Addendum: Updated IR Non-Linearity Coefficients

The `calwf3` implementation of the IR non-linearity correction is a multiplicative increase of signal that takes the form $(1 + \delta)$, where δ is a third-order polynomial of the measured fluence (see §3.3.6 of the *WFC3 Data Handbook* (Pagul and Rivera 2024)). This convention matches that adopted for the *JWST* NIRCam detector (Eq. 5 of Canipe et al. (2017)) and its corresponding reduction pipeline.

Following historical convention (eg., Eq. 4 of Hilbert (2014)), the 2025 pixel-based IR non-linearity fitting determined the third-order polynomial approximation of the fluence *deficit* (Eq. 3 of Shenoy et al. (2025)). Rather than modifying `calwf3` to divide the measured signal by this deficit, the WFC3 Team approximated the multiplicative correction by negating all the polynomial coefficients – essentially making the substitution $(1 + \delta) \approx (1 - \delta)^{-1}$ (see Eqs. 2 and 3 of Shenoy et al. (2025)). This substitution is acceptable when $\delta \ll 1$. However the WFC3 Team subsequently concluded that IR non-linearity becomes large enough at the highest (non-saturated) fluence levels to significantly ($> 0.3\%$) compromise this approximation.

As of February 2026, the WFC3 Team has swapped in a revised set of coefficients, now based on a third-order polynomial fit to the reciprocal of the $(1 - \delta)$ polynomial expansion (rather than just negating the polynomial coefficients). **The updated NLINFILE a2412448i_lin.fits will be used by the calwf3 pipeline for reprocessing all IR observations in Spring 2026.** The WFC3 Team has extensively tested the impact of

the latest revised IR non-linearity coefficients, as summarized in the plots and discussion to follow.

Figure A1 shows the effect of the revised non-linearity coefficients for the case of a single STEP25 INTFLAT selected from Figure 5. The updated coefficients are seen to improve linearity of the flat field ramp at \approx all fluence levels (*green curve*) compared to the ramp based on the 2025 coefficients (*orange curve*), and most noticeably for the highest fluence levels.

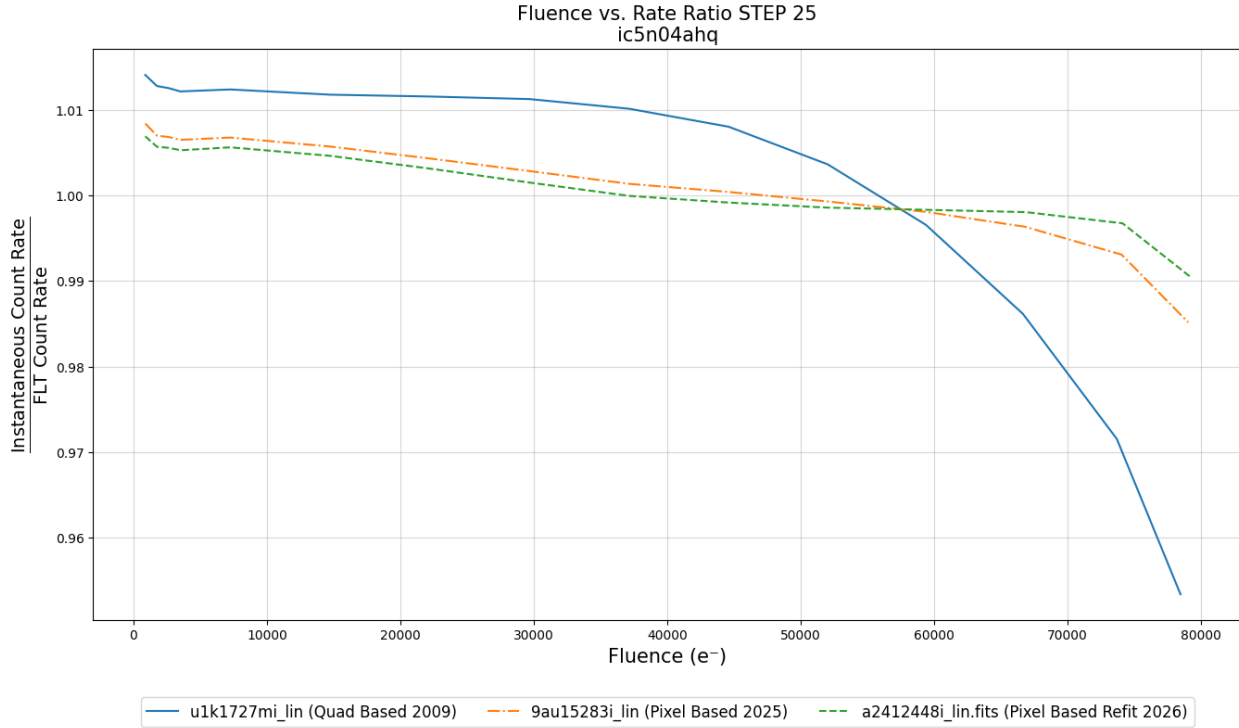


Figure A1: *Similar to Figure 5, but now showing the improvement in the ramp for a representative STEP25 INTFLAT exposure calibrated with the 2026 pixel-based non-linearity reference file (green), the 2025 pixel-based solution (orange), and the 2009 quad-based solution (blue).*

Additional test results using the 2026 revised coefficients are shown in the right panel of Figure A2 for the 47 Tucanae data presented in Figure 10. Small improvements can be seen in the high fluence regime, similar to the results found for INTFLAT data.

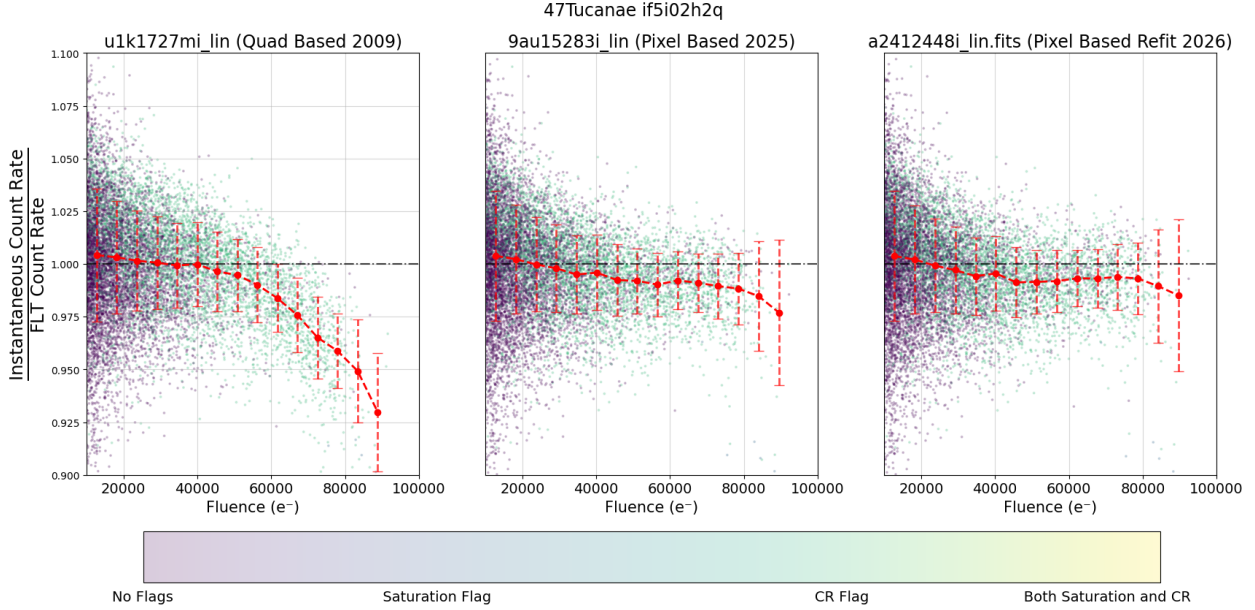


Figure A2: *Similar to Figure 10, but now additionally showing the improvement in the ramp for an image of 47 Tucanae calibrated with the 2026 pixel-based non-linearity reference file (right), compared to the results using the 2025 pixel-based reference file (middle) and the 2009 quad-based solution (left).*

Lastly, the WFC3 Team has tested the impact of the 2026 non-linearity solution on the IR filter zeropoints. In all cases, changes in the mean flux ratio for the five CALSPEC photometric standards are found to be negligible ($<< 0.1\%$) compared to the 2025 solution (M. Marinelli 2025, priv. comm.). This is unsurprising, given that the peak fluence levels of the photometric standard stars fall in a region of Figure A2 ($\sim 60000 \text{ e}^-$) showing minimal change in the observed count rates due to the updated coefficients.